Nucleation and growth kinetics of $\mathrm{Ra_xBa_{1-x}SO_4}$ solid solution in NaCl aqueous solutions

Yoav O. Rosenberg [a,*], Yonatan Sadeh [a], Volker Metz [b], Carlos M. Pina c,d, Jiwchar Ganor a

[a] Department of Geological and Environmental Sciences, Ben-Gurion University of the Negev, P.O.B. 653, Beer Sheva 84105, Israel
[b] Institute for Nuclear Waste Disposal (INE), Karlsruhe Institute of Technology, P.O.B. 3640, 76021 Karlsruhe, Germany
[c] Department of Crystallography and Mineralogy, Complutense University of Madrid, E-28040 Madrid, Spain

[d] Instituto de Geociencias IGEO (UCM-CSIC), c/Jose´ Antonio Novais 2, E-28040 Madrid, Spain

[*] Corresponding author.
E-mail address: yoavoved@gmail.com (Y.O. Rosenberg).

Abstract

Co-precipitation of Ra and Ba in barite (i.e., the formation of a $\mathrm{Ra_xBa_{1-x}SO_4}$ solid solution) has long been established as an important process that has the potential to control Ra concentration. This process is commonly described by a distribution model. Ample studies have shown that the key parameter of this model, the partition coefficient, varies in the range of 1–2 as a function of temperature, salinity and precipitation kinetics of the RaxBa1 xSO4 solid solution. This roughly twofold change in the partition coefficient may lead to large differences in the concentration of dissolved Ra.

The present study systematically investigated the co-precipitation kinetics of the $\mathrm{Ra_xBa_{1-x}SO_4}$ solid solution from aqueous solutions up to 5.9 mol $\mathrm{kg^{-1}_{H_2O}}$ NaCl,circum-neutral pH and at ambient temperature. Laboratory batch experiments designed to follow the nucleation of the RaxBa1 xSO4 solid solution and the co-precipitation kinetics of Ba and Ra from aqueous solutions which were initially supersaturated with respect to barite (degree of supersaturation, $\beta_{\mathrm{barite}} = 20 ^{+}_{-} 2$

The following empirical law describes the dependence of the activity-based partition coefficient, $K''_{D,\mathrm{barite}}$ on the degree of supersaturation, β_{barite}:

$$K''_{D,\mathrm{barite}} = \text{ð } 1{:}99 \pm 0{:}05\text{Þ} - (0.58 \pm 0.06) \cdot \log(\beta_{\mathrm{barite}}).$$

This empirical law is in good agreement with other literature data. The outcomes of the empirical law are compared to the prediction of a model for the nucleation of two-dimensional islands.

INTRODUCTION

Co-precipitation of Ra and Ba in the barite structure (i.e., the formation of a $\mathrm{Ra_xBa_{1-x}SO_4}$ solid solution) is an important process that has been investigated widely during the last hundred years at different temperatures and salini-ties, and both on the laboratory and field scales (Doerner and Hoskins, 1925; Marques, 1934; Gordon and Rowley, 1957; Rosenberg et al., 2011b, 2013). The interest in a quan-titative description of this process is mainly twofold. Firstly, the Ra isotope quartet (^{223}Ra, ^{224} Ra ^{226}Ra ^{228}Ra), with their different half-lives, is a strong geochemi-cal tool for estimating the rates of different processes (e.g., sedimentation rates, mixing rates of water bodies). For example, in the marine environment Ra-bearing barite was used to interpret sedimentation rates (Paytan et al., 1996; Van Beek et al., 2004). Secondly, high concentrations

List of symbols

Symbol	Meaning
$[i]$	Total solution concentration of element i. Solution activity
α_i^v	of species i.
m_i^v	Molality of species i
K°_{sp}	Solubility product of the pure phase. Concentration-based
K'_D	effective partition coefficient. Activity-based effective
K''	partition coefficient. Equilibrium partition coefficient, ionic-
	strength-independent.
K_D	Mole fraction of component k in the solid solution
$X_{k\alpha}$	phase k = Ra or Ba).
γ_i^v	Activity coefficient of species I in the solution. Rational
$+$	activity coefficient of component k in the solid solution
$\gamma_{k\alpha}$	phase.
β_{barite}	Degree of supersaturation of an aqueous solu-tion with respect to pure barite.

Symbols used in the kinetic models of B + S of 2D islands and of spiral growth

Symbol	Meaning
$x = X_{RaSO_4}$	Solid phase composition.
a	Average cell parameter (m^2).
$\bar{A}_{hkl}^{GU}(x)$	Area occupied by a growth unit as a function of the solid composition x (m^2).
$C_{SE,hkl}(x)$	Equilibrium concentration of growth units on the surface (# particles m^{-2})
$d_{hkl}(x)$	Height of the nuclei (m).
D_S	Mean diffusion coefficient for growth units on the crystal face ($\approx 10^{-9}$ m^2 s^{-1}).
$\Delta G_c(x)$	Critical energy for nucleation as a function of the solid composition x (J m^{-1}).
$\Delta G(\rho,x)$	Energy for nucleation as a function of the nucleus radius and of the solid composition (J m^{-1}).
I(x)	Rate for nucleation of critical nuclei as a function of the solid composition x (# of nuclei formed m^{-2} s^{-1}).
n_{hkl}	Number of monomers per unit area on the (hkl) surface (# particles m^{-2}).
k	Boltzmann constant (1.38 × 10^{-23} J/K).
$R^B_{hkl\,+S}(x)$	Growth rate perpendicular to a given crystal-lographic {hkl} face (m sec^{-1}) according to the birth and spread of 2D islands model.
$R_{hkl}^{BCF}(x)$ {hkl} face -	Growth rate perpendicular to a given crystallographic (m sec^{-1}) according to the spiral growth model.
T	Absolute temperature (K).
$X_{S,hkl}$	Mean diffusion distance on the surface in the mean lifetime of an adsorbed growth unit (m).
$v_\infty(x)$	Growth velocity of a straight step as a function of the solid composition x (m s^{-1}).
$\bar{v}$	Average speed of adsorbed growth units diffusing on the crystal surface (m s 1). VGU(x)- Molecular volume of a growth unit (m^3).
β_r	Retardation factor for the incorporation of growth units into a straight step
$\beta(x)$	supersaturation ratio for a solid solution of composition x.
γ_0	Retardation factor for the incorporation of growth units into a kink site.
λ_d	Width of the diffusion layer between the solid and bulk aqueous phases (m).
ξ	Surface fraction occupied by surface adsorbed growth units.
ρ and ρ_c	Island radius and critical nucleus radius (m).
$\sigma_{hkl}(x)$	Interfacial tension free energy originated when a growth unit attaches on a pre-existing crystal (hkl) face of a solid solution of composition x (J m^{-2}).

of radioactive Ra pose an environmental and health con-cern. For example, the formation of a 'radio-barite' scale in the oil production industry is a well-known issue (Hamlat et al., 2003; Bosbach, 2010) of a naturally occurring radioactive material, which is technologically enhanced.

Since dissolved Ra^{2+} is always a trace component with respect to dissolved Ba^{2+}, the co-precipitation process leads to the formation of a dilute solid solution. In such a sce-nario, Raoult's and Henry's laws apply, and it is therefore convenient and practical to describe this process with a dis-tribution model. Traditionally, in such a model the propor-tion between the Ra/Ba ratios in the solid and aqueous phases is considered constant at equilibrium, and this proportion is represented by a partition coefficient, $K_{D,barite}$ = (Ra/Ba)$_{solid}$/([Ra]/[Ba])$_{solution}$ (Curti, 1999). Re-sults of many studies on Ra and Ba co-precipitation show that the observed (i.e., effective) partition coefficient is not constant, but varies between 1 and 1.8 (see Table 2 in Rosenberg et al., 2011b) as a function of temperature (Gordon and Rowley, 1957), salinity (Rosenberg et al., 2011b, 2013) and the precipitation kinetics of the major component, barite (Rosenberg et al., 2011b, 2013). It is important to note that salinity and temperature affect also the equilibrium partition coefficient (in the same manner as a solubility constant of a mineral is affected by them); however, in the case of the Ra$_x$Ba$_{1-x}$SO$_4$ solid solution sys-tem, most of the variation in the effective partition coeffi-cient is due to kinetic effects (Rosenberg et al., 2011b, 2013). It is generally agreed that the value of 1.8 represents the thermodynamic value of the partition coefficient at 25 °C (Doerner and Hoskins, 1925; Bruno et al., 2007). That is, the most stable solid composition will precipitate from a given aqueous composition when $K_{D,barite}$ = 1.8. On the other hand, partition coefficients which are not

Table 1
Initial and final conditions[a] of the three series of experiments.

NaCl (mol $kg^{-1}_{H_2O}$)	~0	1.0	5.9
pH	6.3	7.2	6.5
$[Ba]_{initial}$[b] $= [SO_4]_{initial}$	$(4.7 \pm 0.2)\times10^{-5}$	$(4.15 \pm 0.02)\times10^{-4}$	$(7.13 \pm 0.01) \times 10^{-4}$
$[^{226}Ra]_{initial}$[b]	$(1.3 \pm 0.1)\times10^{-11}$	$(1.6 \pm 0.2)\times10^{-11}$	$(2.8 \pm 0.2) \times 10^{-11}$
Initial β_{barite}	17	18	22
$([^{226}Ra]/[Ba])_{initial}$	$(2.9 \pm 0.3)\times10^{-7}$	$(3.7 \pm 0.4)\times10^{-8}$	$(2.9 \pm 0.2) \times 10^{-8}$
Induction time (h)	586 ± 54	15 ± 2	44 ± 8
Experiment duration (h)	4874	1609	2785
$[Ba]^{c}_{final} = [SO_4]_{final}$	$(2.3 \pm 0.1)\times10^{-5}$	$(1.00 \pm 0.03)\times10^{-4}$	$(1.20 \pm 0.06) \times 10^{-4}$
$[^{226}Ra]_{final}$[c]	$(4.1 \pm 0.2) \times 10^{-12}$	$(2.0 \pm 0.1) \times 10^{-12}$	$(2.0 \pm 0.2) \times 10^{-12}$
Final β_{barite}	4	1.3	0.5[e]
$(\gamma_{Ra^{2+}}/\gamma_{Ba^{2+}})_{solution}$[d]	1.00	0.96	0.75

[a] All concentrations are in mol $kg^{-1}_{H_2O}$.

[b] Initial values of Ba and ^{226}Ra are based on the averaged concentration (± standard deviation) before nucleation commenced.

[c] Final values of Ba and ^{226}Ra are based on the averaged concentration (± standard deviation) of triplicates or quadruplets.

[d] Activity coefficient ratio is calculated according to the Pitzer formalism. Pitzer parameters for $BaCl_2$ and $RaCl_2$ interaction are those of Monnin and Galinier (1988) and Rosenberg et al. (2011a), respectively.

[e] See text for a discussion regarding this presumably undersaturated value of β_{barite}.

constant, and depend on a given solution composition and/or precipitation kinetics, are referred to as effective (or phenomenological) partition coefficients as discussed below.

This roughly twofold change in the partition coefficient may lead to large differences in the concentrations of dis-solved Ra when estimating its concentration with a parti-tion model. For example, Rosenberg et al. (2013) investigated the co-precipitation of Ra and Ba in a large scale field system. In their case study, which is an evaporitic flow-through system, the effective partition coefficient, $K^0_{D;barite}$, was ~1. Consequently, dissolved Ra concentration in the system was up to threefold higher than predicted if $K^0_{D;barite}$ had been 1.8. Rosenberg et al. (2013) concluded that the decrease in $K^0_{D;barite}$ was a result of both ionic strength and the precipitation kinetics. However, a degree of uncertainty still exists when interpreting solid solution reactions based on field observations, due to the possible interferences of other factors such as different cations or dissolved organic matter.

In a batch type scenario the differences in the aqueous concentrations of Ra can be more substantial. To exemplify it, a numerical simulation is presented below. In the simula-tion Ra is removed from the solution through co-precipita-tion with Ba in a batch type reactor; that is, the simulation starts with initial aqueous concentrations of Ra and Ba with no additional input and in each step of the simulation Ra is removed according to $dRa_{solid} = K_{D,barite}\, dBa_{solid}\, ([Ra]/[Ba])_{solution}$. The removal of Ra was simulated twice: for $K_{D,barite}$ = 1.0 and 1.8. Fig. 1 shows the ratio of Ra concen-tration between the two simulations with respect to the rela-tive amounts of Ba that precipitated. The three circles, from left to right, mark the positions where Ra concentration de-creased by one, two and three orders of magnitude in the sim-ulation of $K_{D,barite}$ = 1.8. At these positions of relative Ba removal from solution, the Ra concentration is by a factor of 3–23 lower when calculated with a $K_{D,barite}$ = 1.8 compared to the respective concentration in the simulation for $K_{D,barite}$ = 1.0. Clearly, if one wishes to estimate how Ra concentrations will be lowered through co-precipitation, a more thorough understanding of this process is needed.

In previous work (Rosenberg et al., 2011b, 2013) Ra co-precipitation was investigated in a complex solution, where the ionic strength was increased through evaporation of the solution. The aim of the present study is to systematically investigate the precipitation kinetics of the $Ra_xBa_{1-x}SO_4$ solid solution by increasing ionic strength and precipitation rates without the interference of other ions such as Ca^{2+} and Sr^{2+} and in the absence of evaporation. To this end the co-precipitation kinetics of Ra and Ba was studied in detail in a series of laboratory batch experiments at 25 °C, and the dependence of the partition coefficient on both the salinity of the aqueous phase (10^{-4}, 1.0 and 5.9 mol kg_{H2O}^{-1} NaCl) and the kinetics of barite precipitation is described. To the best of our knowledge, the current study presents the first systematic data on the kinetics of $Ra_xBa_{1-x}SO_4$ solid solution precipitation.

1.1. Distribution model of co-precipitation

A complete list of symbols used throughout this paper is given above.

1.1.1. Effective value of the partition coefficient

Co-precipitation reactions are commonly described using a distribution model based on an effective (empirical) partition coefficient. Traditionally, the basic form of the distribution model is derived using the concentration-based effective partition coefficient (Doerner and Hoskins, 1925).

For the $Ra_xBa_{1-x}SO_4$ solid solution this partition coefficient is equal to:

$$K'_{D,\mathrm{barite}} = \left(\frac{d\mathrm{Ra}}{d\mathrm{Ba}}\right)_{\mathrm{solid}} \Big/ \left(\frac{[\mathrm{Ra}]}{[\mathrm{Ba}]}\right)_{\mathrm{solution}} \quad (1)$$

where $K^0_{D;barite}$ is the concentration-based effective partition coefficient, [i] represents the aqueous concentration of element i (i = Ba or Ra), and disolid represents the concentration-

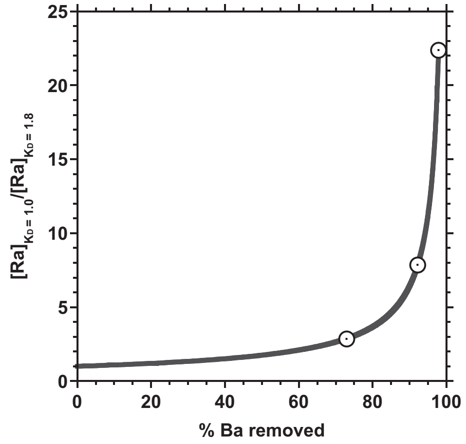

Fig. 1. The ratio of [Ra] concentrations between two simulations of Ra–Ba co-precipitation with respect to the relative amount of Ba that precipitated. The simulations follow the concentrations of Ra and Ba in a batch type system where $K_{D,\text{barite}} = 1.0$ or 1.8. The three circles, from left to right, mark the positions where Ra concentration decreased by 1, 2 and 3 orders of magnitude in the simulation of $K_{D,\text{barite}} = 1.8$. The increase in the ratio of the y axis as more Ba precipitates indicates that the almost twofold difference in the value of $K_{D,\text{barite}}$ may have substantial impact on the remaining concentration of Ra in the solution.

of element i in the *surface* of the solid (mol kg^{-1}_{solid}), indicating that ion partitioning takes place between the solution and the outermost layer of the mineral, and not the bulk of the solid (Curti, 1999).

When the total concentrations are significantly different from the activities it is advisable to replace Eq. (1) by (Langmuir and Riese, 1985):

$$K''_{D,\text{barite}} = \left(\frac{d\text{Ra}}{d\text{Ba}}\right)_{\text{solid}} \Big/ \left(\frac{a_{\text{Ra}^{2+}}}{a_{\text{Ba}^{2+}}}\right)_{\text{solution}} \tag{2}$$

where $K''_{D,\text{barite}}$ is the *activity*-based effective partition coefficient, and a_i^{v+} is the activity of species i^{v+} in the solution; a_i^{v+} is calculated in the present work with the Pitzer formalism (Pitzer, 1991).

The Pitzer formalism assumes that the solution is completely dissociated (i.e., no ion pair speciation is determined to account for the interactions between ions), and hence $\alpha_i^{v+} = \gamma_i^{v+} \cdot [C_i]$, where γ_i^{v+} is the activity coefficient of species i^{v+} in the solution. From the definitions of Eqs. (1) and (2) it then follows that:

$$K''_{D,\text{barite}} = K'_{D,\text{barite}} \Big/ \left(\frac{\gamma_{\text{Ra}^{2+}}}{\gamma_{\text{Ba}^{2+}}}\right)_{\text{solution}} \tag{3}$$

1.1.2. Thermodynamic value of the partition coefficient

Supporting evidence that the thermodynamic value of the partition coefficient is ~1.8 may rise when considering the thermodynamic properties of the end-members. Thermodynamically, the partition coefficient is related to the solubility product of the pure end-members by (McIntire, 1963):

$$K_{D,\text{barite}} = \left(\frac{K^{\circ}_{\text{sp,BaSO}_4}}{K^{\circ}_{\text{sp,RaSO}_4}}\right) \cdot \left(\frac{\gamma_{\text{Ba}^{2+}}}{\gamma_{\text{Ra}^{2+}}}\right) \cdot \gamma_{\text{BaSO}_4} / \gamma_{\text{RaSO}_4}, \tag{4}$$

where K°_{sp} is the solubility product constant of the pure phase end-member, and $\gamma_{i\text{SO}_4}$ is the activity coefficient of component $i\text{SO}_4$ in the solid solution.

The similar ionic radii of Ra^{2+} and Ba^{2+}, their electronegativities and electronic configurations, and the virtually identical crystallographic structures of pure RaSO_4 and barite (Curti, 1999; Zhu, 2004) suggest that the $\text{Ra}_x\text{Ba}_{1-x}\text{SO}_4$ solid solution can be considered as an almost ideal solid solution. Therefore, the ratio of the activity coefficients of the solid components is probably close to unity. In a dilute aqueous solution (i.e., where the ratio of the activity coefficients of the aqueous species is close to unity), the partition coefficient will be roughly equal to:

$$K_{D,\text{barite}} \approx \frac{K^{\circ,\text{BaSO}_4}_{\text{sp}}}{K^{\circ,\text{RaSO}_4}_{\text{sp}}}. \tag{5}$$

Considering that the reported values for the solubility products of the end-members (values of $\log(K^{\circ}_{\text{sp}})$) for barite and pure RaSO_4 are −9.98 and −10.26, respectively, (Rosenberg et al., 2011a and references therein), then the thermodynamic value of $K_{D,\text{barite}}$ according to Eq. (5) is 1.9. This is in agreement with the so-called thermodynamic value which was determined experimentally, 1.8 ± 0.1 (Doerner and Hoskins, 1925).

Alternatively, the $\text{Ra}_x\text{Ba}_{1-x}\text{SO}_4$ solid solution may be considered non-ideal such that the solid activity coefficients can be described as a function of the solid composition using a regular model (Zhu, 2004; Curti et al., 2010). Since we are dealing with a dilute solid solution, then Raoul's law ($\gamma_{\text{BaSO}_4} \approx 1$) and Henry's law ($\gamma_{\text{RaSO}_4}$ is constant) apply. γ_{RaSO_4} can thus be estimated by Eq. (4); assuming that the experimental value of 1.8 ± 0.1 represents the thermodynamic value of $K_{D,\text{barite}}$, and that the ratio of the aqueous activity coefficient is unity (i.e., in a dilute solution), then γ_{RaSO_4} is calculated to be 1.06 ± 0.06 (i.e., within error, the $\text{Ra}_x\text{Ba}_{1-x}\text{SO}_4$ is an ideal solid solution).

2. METHODS

2.1. Experimental setup

All experiments were single point batch experiments (i.e., each experiment bottle was used to determined one data point). Three series of experiments, varied by their NaCl concentrations, were conducted: 1. $\text{NaCl} = 9.410^{-4}$ mol kg^{-1}_{H2O}, 2.$\text{NaCl} = 1.0$ mol $\text{kg}^{-1}_{\text{H2O}}$ and 3.$\text{NaCl} = 5.9$ mol kg^{-1}_{H2O}. In the following, the 9.4×10^{-4} mol $\text{kg}^{-1}_{\text{H2O}}$NaCl series is denoted as " ≈ 0 mol $\text{kg}^{-1}_{\text{H2O}}$ NaCl". Two types of stock solutions, $\text{NaCl} + \text{BaCl}_2$ and $\text{NaCl} + \text{Na}_2\text{SO}_4$, were prepared at the desired concentrations in double distilled water (DDW, >16 MΩ cm^{-1}) from the appropriate salts (Merck, GR grade). All stock solutions were filtered through 0.45 μm membranes (Millipore). The $\text{NaCl} + \text{BaCl}_2$ and $\text{NaCl} + \text{Na}_2\text{SO}_4$ stock solutions were adjusted such that the three experimental series would have a similar degree of supersaturation with respect to pure barite ($\beta_{\text{barite}} = [a^{2+}_{\text{Ba}} \cdot \alpha^{2-}_{\text{SO}_4}]/K^{\circ,\text{BaSO}_4}_{\text{sp}} = 20 \pm 2$). An NIST Standard Reference Material (SRM # 4967A) with a specific ^{226}Ra radioactivity of 2482 Bq g^{-1} was diluted to a specific activity of 20 Bq g^{-1} in 1% nitric acid (Trace select, Fluka). The

$NaCl + BaCl_2$ stock solution of each series was spiked with the diluted ^{226}Ra solution. The pH of the $NaCl + BaCl_2$ ($+RaCl_2$) was adjusted with diluted NaOH to be slightly above 8 such that the mixing of the two stock solutions would result with a circum-neutral pH (Table 1). Prior to the beginning of each series, the two stock solutions were mixed and stirred well to have a final mass of ~10 kg and the time of mixing was recorded as the initial time of each series of experiments. The mixed solution of each series was immediately divided equally into 23 bottles (250 ml polyethylene, Kartell Company), which were then immersed in a shaken thermostatic water bath (25 °C).

For the last sampling point of each series three to four different bottles were sampled in order to evaluate the quality of the repetition of the single point batch experiments. Upon sampling, the entire solution in the given bottle was filtered (0.22 μm). A few ml were then diluted by weight with DDW and acidified to 1% nitric acid for the analysis of Ba, Na, Cl and SO_4. The rest of the solution was diluted in a plastic beaker with distilled water free of radium (DWFR) to a final volume of 2 L for ^{226}Ra sampling, as described below.

2.2. ^{226}Ra analysis

DWFR used for the dilution of each sample was prepared by passing distilled water through 20 g of MnO_x acrylic fibers which efficiently adsorb Ra^{2+} (Scientific Computer Instruments, e.g., Moore, 2008). Following the dilution of each sample, ^{226}Ra was pre-concentrated by immersing 20 g of fresh MnO_x acrylic fibers in the beaker. The fibers were immersed for at least an hour and periodically stirred by hand before they were collected for ^{226}Ra analysis. Each diluted sample was successively passed through additional 10 g of MnO_x acrylic fibers in order to verify that the pre-concentration of ^{226}Ra was quantitative (i.e., that the additional 10 g of MnO_x acrylic fibers do not contain a significant amount of ^{226}Ra).

^{226}Ra measurements were carried out by Radon in Air Monitor (RAD7, Durrige Company). MnO_x fibers of each sample were sealed and incubated for over 3 weeks and then measured by the alpha counter assuming secular equilibrium between ^{226}Ra, ^{222}Rn and the α-emitting radon progeny (^{214}Po and ^{218}Po) (Kim et al., 2001). The radon monitor RAD7 is based on an electrically biased solid state detector for alpha spectrometry of the ^{222}Rn daughters – ^{218}Po (6.002 MeV) and ^{214}Po (7.687 MeV). Any interference of ^{212}Bi (6.08 MeV, ^{232}Th chain) with ^{218}Po is corrected by counting ^{212}Po (8.784 MeV), the direct daughter of ^{212}Bi. The efficiency of the instrument (7%) was calibrated by external standards with known ^{226}Ra activities (NIST, SRM #4966A). The analytical uncertainty (standard deviation) for the radioactivity range of 12–0.2 Bq (1.45×10^{-12}–2.4×10^{-14} mol) was between 3% and 25%, respectively.

2.3. Bulk chemical analyses of solution samples

Concentrations of dissolved ions remaining in the solutions as a function of time after the beginning of the experiments were analysed as follow: Ba and Na were analysed by Inductively Coupled Plasma Atomic Emission Spectroscopy (ICP-AES) with uncertainty better than ±5% (standard deviation). The concentrations of Cl^- (±3%) and SO_4^{2-} (±3%) were measured by Ion Chromatography.

2.4. Analyses of powder samples

Precipitates, which were retained on the 0.22 μm filters at the end of the experiments, were collected and used for solid phase analyses. From each filter of the 5.9 mol $\mathrm{kg}^{-1}_{\mathrm{H2O}}$NaCl experimental series few milligrams of precipitates were recovered; smaller amount of precipitates were recovered from the 1.0 mol $\mathrm{kg}^{-1}_{\mathrm{H2O}}$ experiments, whereas no precipitates could be identified on the filters of the ~0 mol $\mathrm{kg}^{-1}_{\mathrm{H_2O}}$ experimental series. The powder samples of the 1.0 and 5.9 mol $\mathrm{kg}^{-1}_{\mathrm{H_2O}}$ experiments were characterized using scanning electron microscope energy dispersive spectrometry (SEM-EDS) and X-ray diffraction (XRD). The electron microscope studies were carried out using a Quanta 650 FEG instrument (FEI, Eindhoven, The Netherlands) equipped with a Thermo Scientific UltraDry silicon drift X-ray detector. SEM images were acquired at an electron accelerating voltage of 5 kV, and SEM-EDS measurements were made at 30 kV. Data analyses were performed using a NORAN System 7 X-ray microanalysis system for the Quanta 650 FEG instrument. XRD measurements were performed using a D8 Advance diffractometer (Bruker AXS) equipped with a Cu radiation tube and Ni filter, working at an X-ray source current of 25 mA and a voltage of 40 kV. Diffractograms were recorded in the range 2–100° 2Θ with steps of 0.01° 2Θ, 8 s counting time and variable slit widths.

Note that the recovered powder samples were used for the above spectroscopic studies, while both the amount and composition (and hence the Ra/Ba ratio) of the precipitated solid were determined by mass-balance from the chemical analyses of the aqueous solution samples as discussed below.

2.5. Thermodynamic calculations

Ion activities and degrees of saturation were calculated with the geochemical speciation model Phreeqc 2.15 (Parkhurst and Appelo, 1999) using the Pitzer formalism. The thermodynamic data were based on the dataset of Harvie et al. (1984) which was extended for Ba by Monnin and Galinier (1988). The estimated $RaCl_2$ Pitzer parameters of Rosenberg et al. (2011a) were used to calculate the activity coefficient of Ra.

3. RESULTS

3.1. Solutions

Table 1 presents the initial conditions of each series, while Table 2 presents the changes in the measured Ba and ^{226}Ra concentrations and in β_{barite} with time for all the data points. SO_4 concentration was measured in the

Table 2
Measured Ba and ^{226}Ra concentrations[a] and degree of supersaturation for barite (β_{barite}) with time for the three experiments.

NaCl $\approx$ 0 mol $kg_{H_2O}^{-1}$				NaCl = 1.0 mol $kg_{H_2O}^{-1}$				NaCl = 5.9 mol $kg_{H_2O}^{-1}$			
Time (h)	[Ba]	[^{226}Ra]	β_{barite}	Time (h)	[Ba]	[^{226}Ra]	β_{barite}	Time (h)	[Ba]	[^{226}Ra]	β_{barite}
0.25	4.64×10^{-5}	1.43×10^{-11}	16.8	0.35	4.12×10^{-4}	1.64×10^{-11}	21.8	0.2	7.14×10^{-4}	2.14×10^{-11}	17.9
149	4.51×10^{-5}	1.27×10^{-11}	16.4	6.2	4.20×10^{-4}	1.65×10^{-11}	21.1	9.6	7.14×10^{-4}	2.16×10^{-11}	18.3
222	4.63×10^{-5}	1.48×10^{-11}	16.8	8.0	4.15×10^{-4}	1.62×10^{-11}	21.7	12.6	7.16×10^{-4}	1.90×10^{-11}	17.9
268	4.80×10^{-5}	1.45×10^{-11}	17.4	8.9	4.14×10^{-4}	1.56×10^{-11}	21.8	15.4	7.12×10^{-4}	2.03×10^{-11}	17.8
293	4.59×10^{-5}	1.22×10^{-11}	16.7	9.9	4.14×10^{-4}	1.62×10^{-11}	22.1	22	7.13×10^{-4}	1.95×10^{-11}	18.0
345	4.34×10^{-5}	1.40×10^{-11}	15.8	11.6	4.14×10^{-4}	1.47×10^{-11}	21.9	27	7.12×10^{-4}	2.06×10^{-11}	17.8
382	4.54×10^{-5}	1.38×10^{-11}	16.5	13.5	4.09×10^{-4}	1.52×10^{-11}	21.8	32	7.12×10^{-4}	2.06×10^{-11}	17.8
428	4.84×10^{-5}	1.31×10^{-11}	17.5	16.0	3.96×10^{-4}	1.40×10^{-11}	21.8	39	6.95×10^{-4}	2.09×10^{-11}	17.8
499	4.87×10^{-5}	1.22×10^{-11}	18.4	24	3.66×10^{-4}	1.34×10^{-11}	21.8	50	6.73×10^{-4}	1.72×10^{-11}	17.8
547	4.81×10^{-5}	1.25×10^{-11}	18.0	29	3.64×10^{-4}	1.35×10^{-11}	21.3	63	6.37×10^{-4}	1.49×10^{-11}	16.9
624	4.20×10^{-5}	1.21×10^{-11}	13.9	32	3.58×10^{-4}	1.17×10^{-11}	20.0	76	5.92×10^{-4}	1.44×10^{-11}	15.9
697	4.21×10^{-5}	1.19×10^{-11}	13.9	51	2.96×10^{-4}	9.91×10^{-12}	17.0	96	5.62×10^{-4}	1.65×10^{-11}	14.2
836	3.91×10^{-5}	9.60×10^{-12}	12.1	75	2.44×10^{-4}	7.72×10^{-12}	16.8	124	4.48×10^{-4}	1.09×10^{-11}	12.3
992	3.38×10^{-5}	8.90×10^{-12}	9.1	126	1.89×10^{-4}	5.89×10^{-12}	16.3	168	4.16×10^{-4}	1.02×10^{-11}	11.0
1125	3.30×10^{-5}	7.79×10^{-12}	8.7	172	1.75×10^{-4}	4.19×10^{-12}	11.1	216	3.71×10^{-4}	9.15×10^{-12}	7.0
1390	3.93×10^{-5}	1.19×10^{-11}	12.2	254	1.48×10^{-4}	3.60×10^{-12}	7.6	365	2.95×10^{-4}	7.39×10^{-12}	6.1
1634	2.94×10^{-5}	6.63×10^{-12}	6.9	447	1.24×10^{-4}	2.85×10^{-12}	4.6	603	2.11×10^{-4}	4.84×10^{-12}	4.8
2109	3.12×10^{-5}	6.41×10^{-12}	7.8	594	1.08×10^{-4}	2.53×10^{-12}	3.9	1058	1.67×10^{-4}	3.29×10^{-12}	3.0
2662	2.52×10^{-5}	ND[b]	5.1	892	1.02×10^{-4}	2.24×10^{-12}	2.8	1761	1.35×10^{-4}	2.39×10^{-12}	1.5
3718	2.31×10^{-5}	4.08×10^{-12}	4.3	1609	9.47×10^{-5}	1.79×10^{-12}	2.0	1756	1.29×10^{-4}	2.39×10^{-12}	1.0
3718	2.69×10^{-5}	4.62×10^{-12}	5.8	1609	9.93×10^{-5}	1.93×10^{-12}	1.5	1762	1.30×10^{-4}	2.41×10^{-12}	0.6
3718	2.65×10^{-5}	4.97×10^{-12}	5.7	1610	1.03×10^{-4}	1.99×10^{-12}	1.3	2785	1.20×10^{-4}	1.98×10^{-12}	0.5
3718	2.25×10^{-5}	4.81×10^{-12}	4.1	1610	1.03×10^{-4}	2.15×10^{-12}	1.3				
4874	2.26×10^{-5}	4.13×10^{-12}	4.1								

[a] All concentrations are in mol $kg_{H_2O}^{-1}$.

[b] ND – not determined.

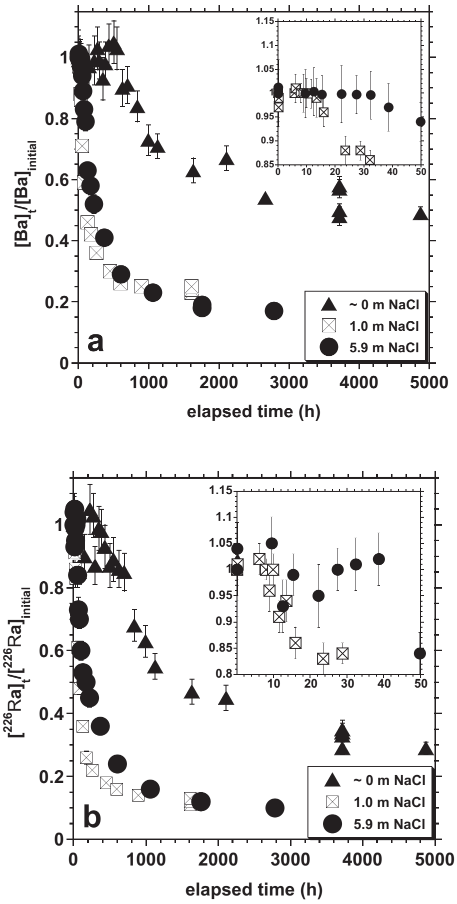

Fig. 2. The relative change in (a) Ba and (b) ^{226}Ra concentrations vs. time for the three series of experiments. The inset of each figure shows the first 50 h where the induction time of the more saline experiments can be noticed.

stock solution that was used to prepare the experiments' solutions and in a few data points along the experiments. The Ba:SO_4 ratio was 1 within 5% and we therefore conclude that the solution was stoichiometric. The change in SO_4 concentration was thus calculated according to the change in Ba concentration. For each series a quadruplet or triplicate was sampled at the final stage of the series (Table 2). These replicates were sampled from different bottles and show a very good reproducibility (standard deviation of Ba and ^{226}Ra measurements was usually much better than 9%). Therefore we conclude that the analytical noise of the single point batch experiments was relatively low.

The relative remaining concentrations of Ba and ^{226}Ra with time in the three series is shown in Fig. 2a and b, respectively; the inset of each figure shows the first 50 h. In the absence of crystallization seeds, some time elapses between the establishment of a supersaturated solution and the detection of a new phase in a system. This time is known as the "induction period" or "induction time" (Söhnel and Mullin, 1988). Induction time, t_{ind}, for nucleation is determined here as the median time (±1 standard deviation) of two consecutive points between which a significant decrease in Ba concentrations (>5%) is observed. The induction times for the three series of ~0, 1.0 and 5.9 mol $kg_{H_2O}^{-1}$ NaCl were 586 ± 54, 15 ± 2 and 44 ± 8 h, respectively. The constant concentrations of Ra and Ba in the experiments prior to the induction times suggest that sorption of these two cations to the bottle wall is an insignificant process in these experiments.

In the experimental series with the lowest salinity the slowest decrease in Ra and Ba concentrations was observed. The experiments were still supersaturated with respect to barite even after 4800 h ($\beta_{barite} = 4$, Table 1). The fastest decrease in Ra and Ba was measured in the experimental series with 1 mol $kg_{H_2O}^{-1}$ NaCl which came near to equilibrium after ~ 850 h. The state "came near-to-equilibrium" was defined when the solution composition in the last two bottles of an experimental series were equal within error. The experiment of 5.9 mol $kg_{H_2O}^{-1}$ NaCl took about 1700 h to come near to equilibrium. Calculation of the degree of saturation unreasonably suggests that after 1700 h the series with 5.9 mol $kg_{H_2O}^{-1}$ NaCl was slightly undersaturated ($\beta_{barite} = 0.5$); this value cannot be explained by considering the analytical uncertainty on solute concentrations. The Pitzer parameters used to calculate the activity coefficient of Ba (Monnin and Galinier, 1988), and therefore to calculate β_{barite}, were originally fitted to solubility data of barite up to NaCl concentration of 5 mol $kg_{H_2O}^{-1}$. Therefore, the calculation of β_{barite} in the most saline experiment in the present work (5.9 mol $kg_{H_2O}^{-1}$ NaCl) is an extrapolation of the Pitzer parameters of Ba, which may introduce error. However, this set of Pitzer parameters is the most accurate for calculation barite solubility at high ionic strengths (see discussion and electronic annex in Rosenberg et al., 2011a).

3.1.1. Solids

In the XRD pattern from a precipitate recovered from the experimental series with 5.9 mol $kg_{H_2O}^{-1}$ NaCl, strong halite peaks are observed besides weak peaks of another mineral. Due to the low intensities of its peaks, the minor phase cannot be identified unambiguously. Solely weak halite peaks are determined in diffractograms of powders collected from filters of the experimental series with 1 mol $kg_{H_2O}^{-1}$ NaCl. Applying the electron backscattering detection mode of the SEM, crystals with relatively higher electron density were detected amongst the halite crystals in powders of the experimental series with 1.0 and 5.9 mol $kg_{H_2O}^{-1}$ NaCl. According to SEM-EDS analyses, the dense crystals consist of $BaSO_4$. Rosulate barite aggregates and barite twins are found besides elongated and tabulated orthomorphic dipyramidal barite crystals. Whereas in samples of the experiments in 5.9 mol $kg_{H_2O}^{-1}$ NaCl mainly idiomorphic barite crystals and aggregates are detected, subhedral barite particles are predominant in samples of the experiments in 1.0 mol $kg_{H_2O}^{-1}$ NaCl. Crystals recovered from both experimental series display split growths on (001) faces, as well as irregular "patches" which are evidence for two dimensional growth. Fig. 3 displays some of the growth features discussed above.

4. DISCUSSION

Differences between t_{ind} observed in the experimental series with ~0, 1.0 and 5.9 mol $kg_{H_2O}^{-1}$ NaCl correlate with the trend in t_{ind} found by He et al. (1995) for barite nucle-

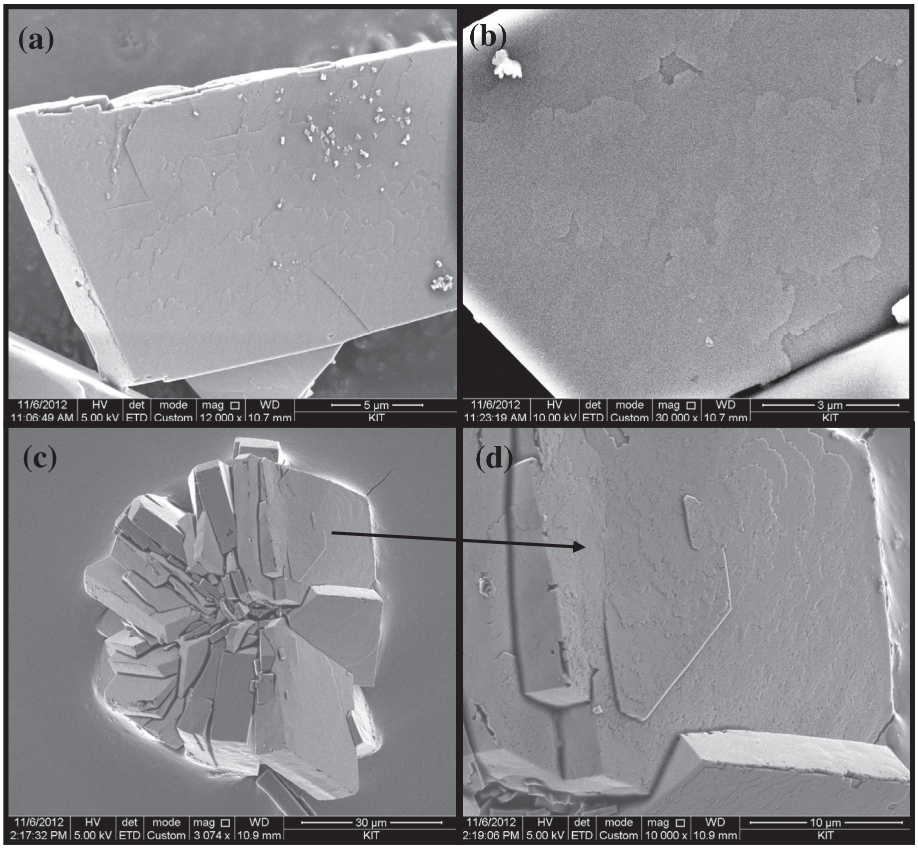

Fig. 3. SEM images of barite crystals showing growth features: (a) a single euhedral barite crystal showing the large (0 0 1) face. The observed irregular "patches" (i.e., *not* the 3D particles concentrated on the top right of the face, which precipitated after removing the crystal from the aqueous solution) are evidence for two-dimensional nucleation. (b) another example of irregular "patches" on a single euhedral barite crystal. Both (a) and (b) images were taken from the series of 5.9 mol $kg_{H_2O}^{-1}$ of NaCl, 95 h after the experiment started (~45 h after t_{ind}) when $\beta_{barite} = 11$. (c) Rosulate barite aggregates. (d) an enlargement of one of the crystals building the rosulate in (d). Irregular "patches" are observed again, this time covering a core of a screw dislocation. Both (c) and (d) images were taken from the series of 5.9 mol $kg_{H_2O}^{-1}$ of NaCl, 365 h after the experiment started (~320 h after t_{ind}) when $\beta_{barite} = 3$.

ation in NaCl solution. As in the present study (Table 1), He et al. (1995) found that t_{ind} in a solution with $\beta_{barite} = 100$ decreased by more than an order of magnitude when NaCl increased from ~0 to 1 mol $kg_{H_2O}^{-1}$ and then increased by a factor of ~2 when NaCl increased to 6 mol $kg_{H_2O}^{-1}$. As discussed by He et al. (1995), the change in nucleation kinetics with salinity is most likely due to changes in barite solubility due to changes in the mean activity coefficient of Ba and SO_4.

4.1. Changes in (Ra/Ba) ratios in the aqueous and solid phases

The amount (mol) of Ba and ^{226}Ra that precipitated was calculated for each time point that followed nucleation according to the change in solute concentrations; the relative amount of ^{226}Ra that precipitated with respect to the final amount of ^{226}Ra that precipitated was then calculated. The changes in [^{226}Ra]/[Ba] and $(^{226}\mathrm{Ra/Ba})_{solid}$ ratios were then plotted against the relative amount of ^{226}Ra that precipitated, representing the progress of the co-precipitation reaction (Figs. 4–6). In each of the three series of experiments, the solution ratio, [^{226}Ra]/[Ba], decreased with the progression of the reaction. The solid ratio, $(^{226}\mathrm{Ra/Ba})_{solid}$, slightly increased in the most diluted NaCl series, and significantly decreased in the series of 1.0 and 5.9 mol $kg_{H_2O}^{-1}$ NaCl. In all three series, however, the solid ratio remained about constant after ~60% of Ra precipitation. This solid ratio remained constant despite the fact that in all three series the solution ratio further decreased after 60% of Ra precipitation (Figs. 4a, 5a and 6a). In a distribution model where a constant partition coefficient is considered, a decrease in the solution ratio should cause a decrease in the solid ratio (i.e., the formation of a concentric compositional zoning in the solid). The constant ratio $(^{226}\mathrm{Ra/Ba})_{solid}$ therefore suggests that a constant partition coefficient is not appropriate to describe the current data.

To further explore this observation, the solid ratio, $(^{226}\mathrm{Ra/Ba})_{solid}$, can be examined through the change in the ratio of the precipitation rates. If the ratio $(^{226}\mathrm{Ra/Ba})_{solid}$ is constant then it follows that the ratio of the precipitation rates is also constant:

$$\frac{d(^{226}\mathrm{Ra})_{solid}/dt}{d(\mathrm{Ba})_{solid}/dt} = \frac{\mathrm{Rate}_{^{226}\mathrm{Ra}}}{\mathrm{Rate}_{\mathrm{Ba}}} = k_I \qquad (6)$$

where k_I is a constant under constant ionic strength I.

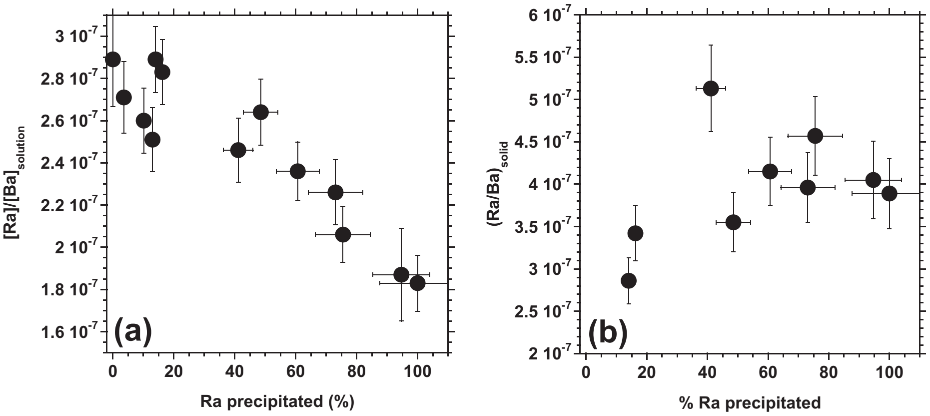

Fig. 4. The change in (a) $[^{226}\mathrm{Ra}]/[\mathrm{Ba}]$ and (b) $(^{226}\mathrm{Ra/Ba})_{\mathrm{solid}}$ ratios vs. the relative amount of precipitated $^{226}\mathrm{Ra}$ for the experiment of ~ 0 mol $\mathrm{kg}^{-1}_{\mathrm{H_2O}}$ NaCl. As the co-precipitation reaction progresses, the solution's $[^{226}\mathrm{Ra}]/[\mathrm{Ba}]$ ratio continuously decreases. Where $^{226}\mathrm{Ra}$ precipitation is above 60% the $(^{226}\mathrm{Ra/Ba})_{\mathrm{solid}}$ ratio remains constant.

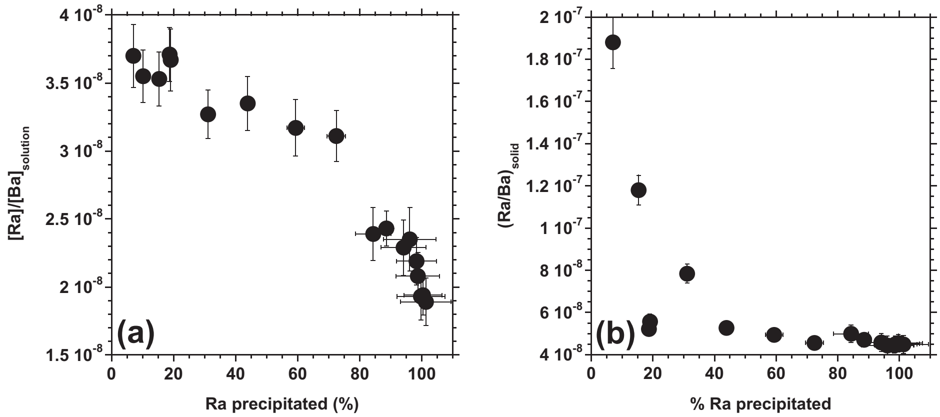

Fig. 5. The change in (a) $[^{226}\mathrm{Ra}]/[\mathrm{Ba}]$ and (b) $(^{226}\mathrm{Ra/Ba})_{\mathrm{solid}}$ ratios vs. the relative amount of precipitated $^{226}\mathrm{Ra}$ for the experiment of 1mol $\mathrm{kg}^{-1}_{\mathrm{H_2O}}$NaCl. As the co-precipitation reaction progresses, the solution $[^{226}\mathrm{Ra}]/[\mathrm{Ba}]$ ratio continuously decreases. Where $^{226}\mathrm{Ra}$ precipitation is above 60% the $(^{226}\mathrm{Ra/Ba})_{\mathrm{solid}}$ ratio remains constant.

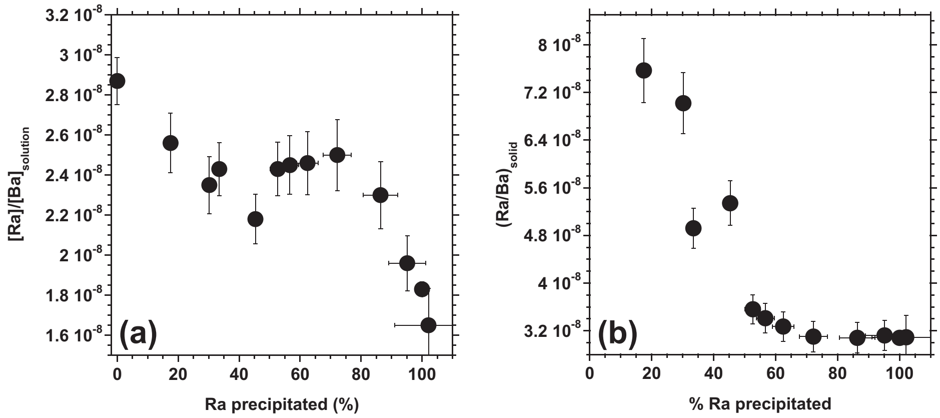

Fig. 6. The change in (a) $[^{226}\mathrm{Ra}]/[\mathrm{Ba}]$ and (b) $(^{226}\mathrm{Ra/Ba})_{\mathrm{solid}}$ ratios vs. the relative amount of precipitated $^{226}\mathrm{Ra}$ for the experiment of 5.9 mol $\mathrm{kg}^{-1}_{\mathrm{H_2O}}$NaCl. As the co-precipitation reaction progresses, the solution $[^{226}\mathrm{Ra}]/[\mathrm{Ba}]$ ratio continuously decreases. Where $^{226}\mathrm{Ra}$ precipitation is above 60% the $(^{226}\mathrm{Ra/Ba})_{\mathrm{solid}}$ ratio remains constant.

A normalized precipitation rate of Ba (and ^{226}Ra) for each time point was calculated using the slope of the linear regression line between the concentrations of dissolved Ba (or ^{226}Ra) and time for each 3 consecutive points as:

$$\mathrm{Rate}_M = \mathrm{Slope}([M];t)\cdot\frac{m_{\mathrm{sol}}}{m_{\mathrm{barite}}}, \tag{7}$$

where $[M]$ denotes aqueous concentration of either Ba or ^{226}Ra, Rate_M is the normalized precipitation rate (mol $\mathrm{sec}^{-1}\mathrm{g}^{-1}_{\mathrm{barite}}$), and m_{sol} and m_{barite} are the solution mass (kg) and barite mass (g), the latter being calculated according to the change in Ba concentration. The calculation in Eq. (7) refers to the second time point of each triplet, and its error can be calculated as the standard error of the slope.

The precipitation rate of ^{226}Ra is plotted against that of Ba in Fig. 7 for each series of experiments on a log–log scale. On such a scale Eq. (6) will have the form:

$$\log(\mathrm{Rate}_{^{226}\mathrm{Ra}}) = \log(\mathrm{Rate}_{\mathrm{Ba}}) + \log(K_I) \tag{8}$$

The data of the precipitation rates was fitted to this linear regression. Data points from the *beginning* of each experiment, which did not fall close to this regression (i.e., where the ratio $(^{226}\mathrm{Ra/Ba})_{\mathrm{solid}}$ is not approximately constant), were excluded from it and are marked by open circles in Fig. 7. The almost perfect linear regressions in Fig. 7 demonstrates that during most of the precipitation process the ratio $(^{226}\mathrm{Ra/Ba})_{\mathrm{solid}}$ is constant. Note that the ratio $(^{226}\mathrm{Ra/Ba})_{\mathrm{solid}}$ (calculated by mass balance) represents the cumulative ratio of ^{226}Ra to Ba, which is affected by the history of the precipitation of each solute, while the ratio $(\mathrm{Rate}_{^{226}Ra}/\mathrm{Rate}_{\mathrm{Ba}})$ represents the incremental ratio of the solutes in the solid. This is why more data points appear to have no constant ratio in Figs. 4b, 5b and 6b than in Fig. 7.

The open circles in Fig. 7 lie above the regression line and therefore represent a higher ratio $(^{226}\mathrm{Ra/Ba})_{\mathrm{solid}}$ at the beginning of the experiments. It therefore appears that the higher ratio $(^{226}\mathrm{Ra/Ba})_{\mathrm{solid}}$ is related to the nucleation process, or, more conservatively stated, to the crystal growth process when the crystals are very small.

4.2. The dependence of the partition coefficient on β_{barite} and ionic strength

Combining Eqs. (1) and (6) the following empirical relation can be written:

$$K'_{D,\mathrm{barite}} = k_I\cdot\frac{[Ba]}{[^{226}\mathrm{Ra}]} \tag{9}$$

Equation (9) is an empirically-derived expression that describes the present experimental data; k_I is used to calculate the changes in $K'_{D,\mathrm{barite}}$, but its significance only applies to the presented experimental data. These changes are described below by more fundamental parameters.

$K'_{D,\mathrm{barite}}$ was calculated for each time point that had a constant $(\mathrm{Rate}_{^{226}Ra}/\mathrm{Rate}_{\mathrm{Ba}})$ ratio according to Eq. (9) and the respective k_I that was estimated by the linear regressions in Fig. 7 (solid lines). The results are plotted against the experimental β_{barite} in Fig. 8a (i.e., against the evolution of β_{barite} with time).

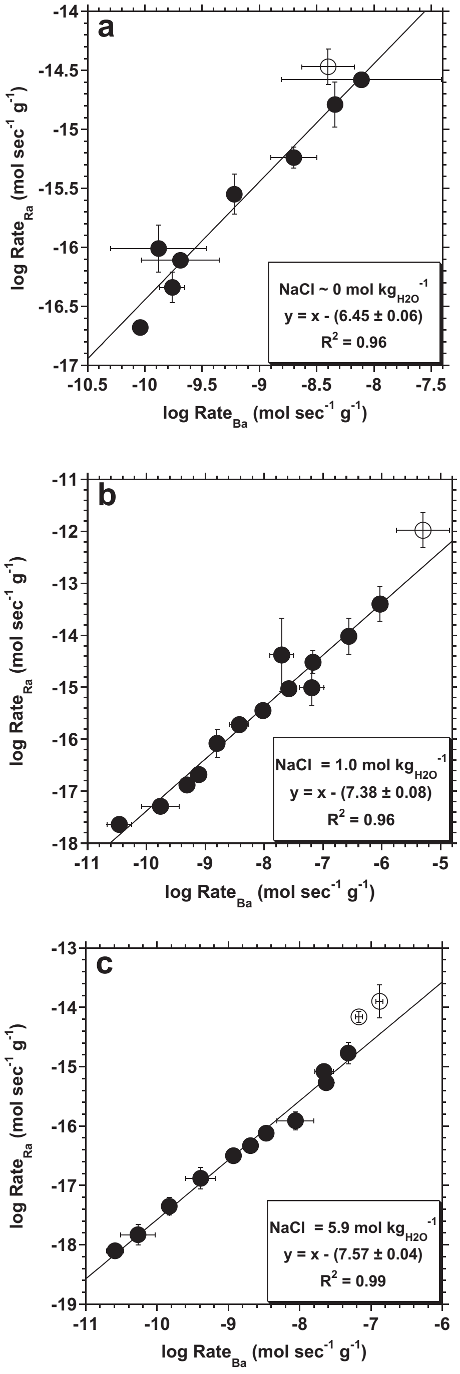

Fig. 7. Precipitation rate of ^{226}Ra vs. that of Ba on a log–log scale for the experiments of: (a) ~0 mol $\mathrm{kg}^{-1}_{\mathrm{H_2O}}$NaCl, (b) 1.0 mol $\mathrm{kg}^{-1}_{\mathrm{H_2O}}$NaCl, and (c) 5.9 mol $\mathrm{kg}^{-1}_{\mathrm{H_2O}}$NaCl. Precipitation rates (mol $\mathrm{sec}^{-1}\mathrm{g}^{-1}_{\mathrm{barite}}$) were calculated according to Eq. (7). Linear regression is shown for the closed circles and represents a constant ratio $(\mathrm{Ra/Ba})_{\mathrm{solid}}$ in the solid (Eq. (8)), while the open circles represent a higher ratio at the beginning of each of the experiments.

The experimental data show two clear trends: (a) For each series $K'_{D,\mathrm{barite}}$ decreases as β_{barite} increases (i.e., less $\mathrm{RaSO_4}$ in the solid); this resembles the kinetic effect on the co-precipitation reaction, where the more soluble phase composition (i.e., more $\mathrm{BaSO_4}$ in the solid) tends to in-

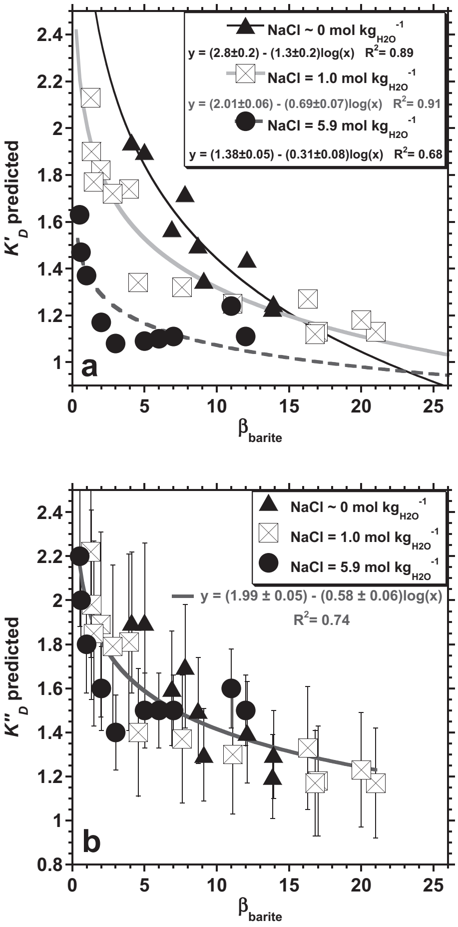

Fig. 8. The dependence of the effective partition coefficient on the degree of supersaturation of the solution with respect to barite: (a) The dependence of the concentration-based partition coefficient, $K'_{D,\text{barite}}$, shows that for each series $K'_{D,\text{barite}}$ decreases as β_{barite} increases (i.e., a kinetic effect on the co-precipitation reaction) and that for a given β_{barite} it decreases with the increase of NaCl concentration (i.e., an ionic strength effect). (b) The dependence of $K''_{D,\text{barite}}$ on β_{barite} is free of the ionic strength effect and shows only the kinetic effect on the co-precipitation reaction. The non-linear regression is through all the data points and represents an empirical law for the calculation of $K''_{D,\text{barite}}$ according to β_{barite} (Eq. (10)).

crease the precipitation rate (Pina and Putnis, 2002); (b) For a given β_{barite} the concentration-based partition coefficient, $K'_{D,\text{barite}}$, decreases with the increase of NaCl concentration. This trend resembles the ionic strength effect on the co-precipitation (Rosenberg et al., 2011a). As the kinetic effect increases (i.e., above β_{barite} of 10) the ionic strength effect is less dominant and the experimental data of all series converge. For clarity, the error bars of the experimental data were omitted from Fig. 8a. However, the significance of the ionic strength effect can be demonstrated by the best fit logarithmic regression (lines) of each series data. Within error these regression lines are significantly different from each other (see regression equations within the plot of Fig. 8a).

The ionic strength effect is the result of non-equal changes in the chemical potential of Ra and Ba produced by the increase in NaCl concentration. This is demonstrated by the decrease in the activity coefficient ratio, $(\gamma^{2+}_{R\alpha}/\gamma^{2+}_{B\alpha})_{\text{solution}}$, with the increase in NaCl concentration (Table 1). This effect can be compensated for by calculating the activity-based partition coefficient, $K''_{D,\text{barite}}$, with Eq. (3). Fig. 8b shows the calculated $K''_{D,\text{barite}}$ with respect to β_{barite}. As can be seen, the data points from the three series of experiments overlap throughout the entire range of β_{barite} regardless of their ionic strengths. The solid line represents the best fit logarithmic regression through all the data points, which now describes only the kinetic effect on the partition coefficient. This agreement among the points of the three series was achieved by using the theoretically based $RaCl_2$ Pitzer parameters of Rosenberg et al. (2011a). Therefore, the present study gives strong experimental support for this set of Pitzer parameters and shows empirically that the common assumption that $(\gamma_{R\alpha^{2+}}/\gamma_{B\alpha^{2+}})_{\text{solution}} = 1$ is not valid under conditions of high ionic strength.

4.3. Agreement between the empirical law and other literature data

Based on the best fit logarithmic regression between $K''_{D,\text{barite}}$ and β_{barite} the following empirical law may be used to calculate the *activity*-based effective partition coefficient (± the uncertainty) for Ra in barite in a solution that is supersaturated with respect to barite:

$$K''_{D,\text{barite}} = (1.99 \pm 0.05) - (0.58 \pm 0.06) \cdot \log(\beta_{\text{barite}}) \qquad (10)$$

This empirical law suggests that as the solution approaches equilibrium with respect to barite, the value of $K''_{D,\text{barite}}$ approaches 1.99 ± 0.05, which is in reasonable agreement with the so-called equilibrium value of the partition coefficient (1.8 ± 0.1).

To further confirm the empirical law in Eq. (10) we compared it with available experimental data. To the best of our knowledge the only data that adequately describes the kinetics of Ra and Ba co-precipitation is that of Rosenberg et al. (2011b) and Rosenberg et al. (2013). Both studies describe the removal of Ra from reject brine of a desalination plant through its evaporation. Rosenberg et al. (2011b) have studied it by evaporating the brine in small scale laboratory batch experiments, while Rosenberg et al. (2013) conducted a field study in the evaporation ponds in which the reject brine is being discarded.

Fig. 9 presents a comparison between the empirical law derived in this study (Eq. (10)) and the data of Rosenberg et al. (2011b) and Rosenberg et al. (2013). The empirical thermodynamic value of the partition coefficient (1.8 ± 0.1, Doerner and Hoskins, 1925), which is in agreement with the thermodynamic value that was calculated using the ratio between the solubility products of the end-members (Eq. (5)), is also plotted against $\beta_{\text{barite}} = 1$. It is important to stress that the solid line in the figure was calculated using only the empirical equation that was derived from the data of the present study, and was not fitted to the data presented in Fig. 9. Nevertheless, the agreement between the derived empirical law and the above literature data is reasonably good. This agreement is despite the fact that the data of Rosenberg et al. (2011b) and Rosenberg

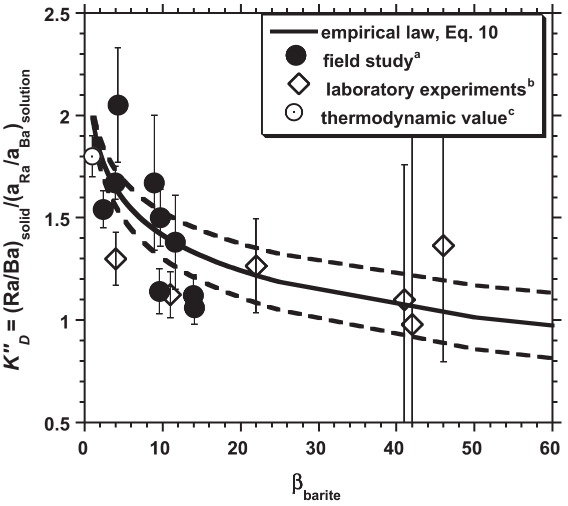

Fig. 9. Comparison between the empirical law (lines, Eq. (10)) for the kinetic effect on $K''_{D,\text{barite}}$ and: (a) field study of Rosenberg et al. (2013) and (b) laboratory study of Rosenberg et al. (2011b). (c) The thermodynamic value of the partition coefficient (1.8, Doerner and Hoskins, 1925) is also plotted against $\beta_{\text{barite}} = 1$. The dashed lines represent the uncertainty envelope on the empirical law in Eq. (10).

et al. (2013) represent studies of higher complexity than the present study (e.g., non-stoichiometric Ba/SO_4 ratios, multi-component chemistry, precipitation of other phases, different solid/liquid ratios, different precipitation kinetics of the barite crystals and precipitation during evaporation). The agreement with the empirical law for $K''_{D,\text{barite}}$ in NaCl solutions implies that the kinetic effect on the precipitation of $Ra_xBa_{1-x}SO_4$ can be adequately described by knowing only the degree of saturation of the solution with respect to pure barite (β_{barite}), a variable which can be readily calculated even in more complex systems. Note that some of the literature data plot above the range of β_{barite} (>22) studied in the present work and thus represent an extrapolation of the rate law.

The overall trend depicted in Fig. 9 is that the value of $K''_{D,\text{barite}}$ slowly approaches a value of unity as the solution is further from equilibrium. In crystal growth, the boundary layer effect accounts for difference between the concentrations of the bulk solution and that of the solution adjacent to the crystal surface. Using this concept, the deviation of the partition coefficient from its thermodynamic value was described by models that considered either the degree of saturation (McIntire, 1963) or the precipitation rate (Wang and Xu, 2001) of the host mineral phase. Both models predict that the partition coefficient will approach unity when the reaction is far from equilibrium. Another model that deals with the kinetic of co-precipitation of trace elements is that of Watson (e.g., Watson, 2004). The premise of the Watson model is that the partitioning of the trace element in the solid phase is an outcome of the competition between crystal growth (which can "trap" surface enriched elements in the crystal lattice) and ion migration in the near-surface region. Alternatively to these models, Pina et al. (2004a) proposed a model for the crystal growth of solid solutions which assumes that the precipitation rate of the solid solution is a function of the solid composition. The model of Pina et al. (2004a) is used below to further interpret the observations of the present study. The model of Pina et al. (2004a) examines the kinetic effect as a function of the solid solution; thus, it is easier to examine the kinetic effect on the partition coefficient which reflects the composition both of the solution and the solid.

4.4. Theoretical model for crystal growth of $Ra_xBa_{1-x}SO_4$ solid solution

4.4.1. Model description

Barite, as well as the barite–celestite solid solution, were used as model systems to study mineral precipitation at the molecular level (Bosbach et al., 1998; Pina et al., 1998; Pina et al., 2000; Risthaus et al., 2001; Bosbach, 2002; Pina and Putnis, 2002; Pina et al., 2004a,b). At the molecular level it has been shown that barite (001) face grows by two distinctive mechanisms: (a) birth and spread of two-dimensional islands and (b) spiral growth (Pina et al., 1998; Bosbach, 2002). For pure barite two-dimensional nucleation is the dominant growth mechanism above supersaturation of $\beta_{\text{barite}} \sim 7\text{–}9$ (Pina et al., 2000, 2004a). As the reaction approaches equilibrium spiral growth becomes a more pronounced growth mechanism. However, due to self-limitation of the spirals (Pina et al., 1998) it may remain a non-effective growth mechanism.

Pina et al. (2004a) have generalized the growth equations of Ohara and Reid (1973) to describe the growth rate (R_{hkl}, m s^{-1}) perpendicular to a given crystallographic $\{hkl\}$ face, by the above mentioned two mechanisms. For the birth and spread of two-dimensional islands model, the growth rate as a function of the solid solution composition can be expressed by (Ohara and Reid, 1973; Pina et al., 2004a):

$$\begin{aligned} R_{hkl}^{B+S}(x) &= 2 \cdot \sqrt[6]{d_{hkl}(x) \cdot (V_{\text{GU}}(x))^5} \\ &\quad \cdot \sqrt[3]{\frac{\bar{v}}{\pi} \cdot \left(n_{hkl}(x) \cdot D_S \cdot \frac{C_{SE,hkl}(x)}{X_{S,hkl}} \right)^2} \\ &\quad \cdot \sqrt[3]{(\beta(x)-1)^2} \cdot \sqrt[6]{(\ln\beta(x))} \\ &\quad \cdot \exp\left(\frac{-\pi \cdot d_{hkl}(x) \cdot (\sigma_{hkl}(x))^2 \cdot V_{\text{GU}}(x)}{3 \cdot (k \cdot T)^2 \cdot \ln\beta(x)} \right) \end{aligned} \tag{11}$$

The rate law for the spiral growth model relies on the BCF theory (Burton et al., 1951) and can be expressed by (Pina et al., 2004a):

$$\begin{aligned} R_{hkl}^{\text{BCF}}(x) &= \frac{2 \cdot D_S \cdot C_{SE,hkl}(x) \cdot k \cdot T \cdot \beta_r \cdot \gamma_0}{19 \cdot X_{S,hkl} \cdot \sigma_{hkl}(x)} \cdot \ln\beta(x) \cdot (\beta(x)-1) \\ &\quad \cdot \tan h\left(\frac{19 \cdot \sigma_{hkl}(x) \cdot V_{\text{GU}}(x)}{2 \cdot k \cdot T \cdot \ln\beta(x) \cdot X_{S,hkl}} \right) \end{aligned} \tag{12}$$

In Eqs. (11) and (12) the argument (x) defines most of the parameters in the rate laws as variables that depend on the solid composition ($x = X_{\text{RaSO}_4}$, the molar fraction of the $RaSO_4$ in the solid solution). d_{hkl} is the height of the nuclei (i.e., a multiple or submultiple of the interplanar dis-

Table 3
Model parameters used to calculate the growth rates, R_{Shkl}^{B+} and R_{hkl}^{BCF} and the free energy for 2D nucleation.

NaCl	a^{a} (Å)	b^{a} (Å)	$c^{a,b} = 2 \cdot d_{hkl}$ (Å)	$V_{GU}{}^{c}$ (m^3)	$\sigma_{hkl} = \sigma_{bulk}{}^{d}$ ($J\ m^{-1}$)	$\lambda_d \approx d_{hkl}{}^{e}$ (Å)	$Ds.$ ^{f} ($m^2\ s^{-1}$)	$\bar{v}$ ^{f} ($m\ s^{-1}$)	K_{sp}° ^{g}
Barite	8.884	5.457	7.156	8.64^{-29}	0.124	3.578	10^{-9}	10^{4}	$10^{-9.98}$
$RaSO_4$	9.16	5.55	7.30	9.28^{-29}	0.126	3.65	10^{-9}	10^{4}	$10^{-10.26}$

[a] The cell parameters, a, b and c are from Hartman and Strom (1989) for barite and Weigel and Trinkel (1968) for $RaSO_4$.

[b] $d_{hkl} = c/2$ as the two-dimensional nuclei have a half unit cell in height (Pina et al., 1998).

[c] V_{GU} calculated as ¼ of the unit cell volume as each unit cell has four growth units ($BaSO_4$ molecules) (Hill, 1977).

[d] Interfacial tension estimated for barite and $RaSO_4$ according to Söhnel (1982).

[e] λ_d, the width of the diffusion layer, is estimated to be equal to the height of the unit cell.

[f] Ds, the diffusion coefficient of the growth units on the crystal face, and $\bar{v}$, the average speed of adsorbed growth units diffusing on the crystal surface, are taken from Pina et al. (2004a).

[g] Solubility constant are from Blount (1977) and Langmuir and Riese (1985) for barite and $RaSO_4$, respectively.

tance of the growing face); V_{GU} is the molecular volume of a growth unit; $\bar{v}$ is the average speed of adsorbed growth units diffusing on the crystal surface; β is the degree of supersaturation; $C_{SE,hkl}$ is the equilibrium concentration of growth units on the surface; n_{hkl} is the number of monomers per unit area on the (hkl) surface (both $C_{SE,hkl}$ and n_{hkl} are expressed in particles/unit area); Ds is the diffusion coefficient of the growth units on the crystal face; $X_{S,hkl}$ is the mean diffusion distance on the surface in the mean lifetime of an adsorbed growth unit; σ_{hkl} is the interfacial free energy of the (hkl) face; β_r and γ_0 are the retardation factors for the incorporation of growth units into a straight step and a kink site, respectively. Finally, k is the Boltzmann constant (1.38×10^{-23} J/K) and T is the absolute temperature.

The change in the degree of supersaturation with the solid composition is probably the most important variable in Eqs. (11) and (12) (Pina et al., 2000, 2004a). Originally, Ohara and Reid (1973) defined the degree of supersaturation as the ratio between the actual concentration of the solute in the solution (e.g., [Ba]) and its equilibrium concentration (i.e., $[Ba]_{solution}/[Ba]_{equilibrium}$). However, in the case of electrolyte solutions the supersaturation represents the true driving force for crystallization only when it is calculated with the activities of the solutes (e.g., Prieto, 2009; Pina and Jordan, 2010). For solid solutions, two generalizations for the calculation of the degree of supersaturation have been proposed, the $\beta(x)$ and $\delta(x)$ functions (Prieto et al., 1993; Astilleros et al., 2003; Prieto, 2009). Although Pina et al. (2004a) proposed the use of the $\delta(x)$ function in Eqs. (11) and (12), we found in our investigation that the simpler $\beta(x)$ function gave satisfactory results (see discussion below). For the $Ra_xBa_{1-x}SO_4$ solid solution the $\beta(x)$ function is calculated as (Prieto et al., 1993):

$$\beta(x) = \frac{(m_{Ra^{2+}} \cdot \gamma_{Ra^{2+}})^{x} \cdot (m_{Ba^{2+}} \cdot \gamma_{Ba^{2+}})^{(1-x)} (m_{SO_4^{2-}} \cdot \gamma_{SO_4^{2-}})}{(K^{\circ}_{sp,RaSO_4} \cdot \gamma_{RaSO_4} \cdot X_{RaSO_4})^{x} \cdot (K^{\circ}_{sp,barite} \cdot \gamma_{BaSO_4} \cdot X_{BaSO_4})^{(1-x)}} \tag{13}$$

It should be noted that the generalization of β, i.e., the $\beta(x)$ supersaturation function given by Eq. (13), does not represent a strict thermodynamic supersaturation of a given aqueous solution to all solid solution compositions; rather, it represents "stoichiometric" supersaturation, in which the solid solution behaves like a pure solid that dissolves or precipitates congruently (see Prieto, 2009). Despite this limitation, $\beta(x)$ has been demonstrated to have practical applications and to be particularly useful in describing nucleation experiments (e.g., Pina et al., 2000; Pina and Putnis, 2002; Rosenberg et al., 2011b).

The parameters V_{GU} and d_{hkl} are considered to vary linearly with the solid composition from one end member to the other. $C_{SE,hkl}$, n_{hkl} and $X_{S,hkl}$ are calculated according to (Pina et al., 2004a):

$$C_{SE,hkl}(x) = \sqrt{K^{\circ}_{sp}(x)} \cdot \lambda_d; \tag{14}$$

$$n_{hkl}(x) \approx \frac{\xi}{A^{GU}_{hkl}(x)} \tag{15}$$

and

$$X_{S,hkl}(x) = 10^{3} \cdot \bar{a} \tag{16}$$

where λ_d is the width of the diffusion layer, used to provide an estimate of the equilibrium concentration of growth units on the (hkl) surface, and is estimated here to be equal to the height of the unit cell (d_{hkl}); ξ is the fraction occupied by surface adsorbed growth units, which is assumed to be equal to unity; $A^{GU}_{hkl}(x)$ is the area occupied by a growth unit as a function of the solid composition, i.e., calculated from the variation of the lattice parameters; and $\bar{a}$ is the average cell parameter.

σ_{hkl}, the interfacial tension between a solid (hkl) face and the aqueous phase, is another important parameter which probably changes both with the solid and solution compositions, and is estimated here from the bulk properties. However, the value of the bulk interfacial tension of barite in dilute solutions varies in the literature between 25 and 140 mJ m^{-2} (Hina and Nancollas, 2000); this range is much larger than the change in σ_{bulk} for barite with ionic strength reported by He et al. (1995) when increasing NaCl concentration up to 1 mol $kg^{-1}_{H_2O}$ (σ_{bulk} decreased from 93 to 79 mJ m^{-2}). To the best of our knowledge no experimental measurements where conducted to estimate σ_{bulk} for $RaSO_4$. Therefore, we chose the empirical relation of Söhnel (1982) to estimate σ_{bulk} for both end members. This empirical relation relates σ_{bulk} to the solubility of the end members, but it also depends on certain assumptions such as the shape factor of the nuclei, and the expression chosen for the driving force. Although these dependencies are identical in the current model and the comprehensive work of Söhnel (1982) it does represent a reasonable approximation between the relative values of the interfacial tension of the

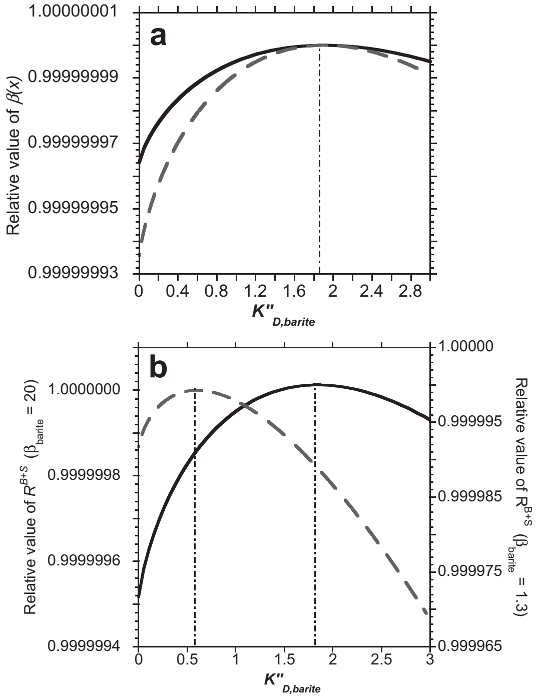

Fig. 10. The relative change in (a) the supersaturation function, β(x), and in (b) the growth rate calculated by the birth and spread model, $R^{B+S}(x)$, as a function of the activity based partition coefficient, $K''_{D,\text{barite}}$, for two aqueous solutions. The two aqueous solutions mainly differ in their distance from equilibrium; with respect to pure barite $\beta_{\text{barite}} = 1.3$ and 20 for the solid and the dashed lines, respectively. The maximum growth rate, $R^{B+S}(x)_{\max}$, represents a solid solution composition that is kinetically likely to precipitate. Very small differences in the y-axis are expected (see text), but produce a significant difference between the solid compositions for which $R^{B+S}(x)$ and $\beta(x)$ are maximal when the system is far from equilibrium. Note that $R^{B+S}(x)_{\max}$ and $\beta(x)_{\max}$ do not correspond to the same solid solution composition, i.e., to the same partitioning coefficient.

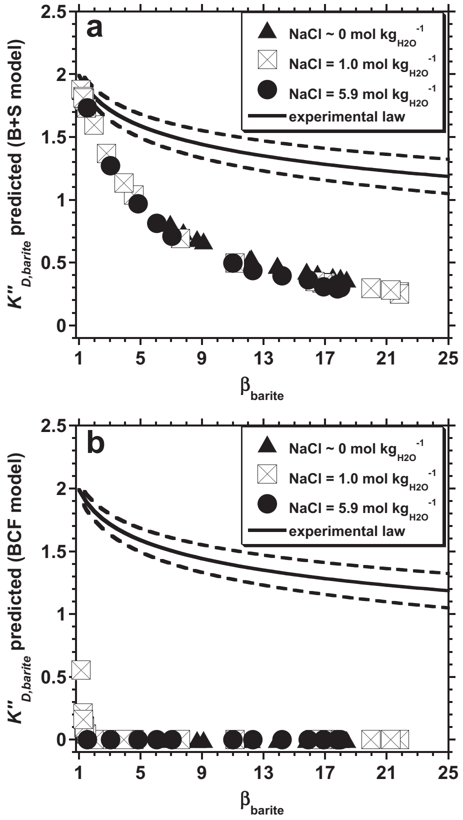

Fig. 11. The activity-based partition coefficient, $K''_{D,\text{barite}}$, as a function of the degree of supersaturation with respect to barite, β_{barite}. Symbols are model results where for each data point the growth rate as a function of the solid composition was calculated according to: (a) birth and spread model (Eq. (11)), and (b) spiral growth (BCF) model (Eq. (12)). The value of $K''_{D,\text{barite}}$ for each calculation is the one which corresponds with the maximum growth rate (see for example Fig. 10). For the BCF model a maximum growth rate was usually calculated for pure barite (i.e., $K''_{D,\text{barite}} = 0$). The solid and dashed lines in both plots are the empirical law and its uncertainty envelop (Eq. (10)).

two pure members. Moreover, the value for σ_{barite} estimated by this relation (124 mJ m^{-2}) is within the range of experimental values given above.

The parameters $\bar{v}$ and Ds. where taken as 10^4 m s^{-1} and 10^9 m^2 s^{-1}, respectively, and both retardation factors, β_r and γ_0, where approximated to unity, as proposed by Pina et al. (2004a) for the similar $Sr_xBa_{1-x}SO_4$–H_2O system. Table 3 summarizes the values of the different parameters used for calculating Eqs. (11) and (12). All the calculations were conducted for the case of growth on the (001) face of the $Ra_xBa_{1-x}SO_4$ solid solution. Since (001) face is one of the most morphologically important faces in barite crystals, the calculations presented and discussed below can be considered representative of the effect of crystal growth kinetics on partition coefficients.

4.4.2. Model results and discussion

The properties of the end members in the $Ra_xBa_{1-x}SO_4$ solid solution (e.g., solubility, unit cell dimensions, etc.) are similar (Table 3). Moreover, the present study investigated the dilute region of this solid solution. Therefore, neither $\beta(x)$ nor $R_{hkl}(x)$ (Eqs. (11) – (13)) should change much with the solid composition, but their values are maximized for a certain solid composition (i.e., certain value of K''_D). Additionally, their values should be similar to the values of the pure barite end-member. Fig. 10a presents the change in $\beta(x)$ relative to its maximum value ($\beta(x)_{\max}$) with respect to the change in K''_D for two representative aqueous solution compositions (i.e., K''_D corresponds to a change in X_{RaSO_4} in the range 0–1 × 10^{-7}). One aqueous solution is far from equilibrium with respect to pure barite (dashed line: $\beta_{\text{barite}} = 20$, $a_{\text{Ba}^{2+}} = 7.5 \times 10^{-5}$, $a_{\text{SO}_4^{2-}} = 2.9 \times 10^{-5}$, $a_{\text{Ra}^{2+}} = 2.5 \times 10^{-12}$), and the other is closer to equilibrium (solid line $\beta_{\text{barite}} = 1.3$, $a_{\text{Ba}^{2+}} = 1.9 \times 10^{-5}$, $a_{\text{SO}_4^{2-}} = 7.2 \times 10^{-6}$, $a_{\text{Ra}^{2+}} = 3.6 \times 10^{-13}$). For both aqueous solutions the function has a maximum which corresponds to the thermodynamic value of the partition coefficient (1.8). Fig. 10b demonstrates the relative change in the rate of the birth and spread growth model, $R^{B+S}_{hkl}(x)$, for the same two aqueous solutions. The maxima of the growth rates of the two aqueous solutions do not coincide with the same partition coefficients – for the aqueous solution which is far from equilibrium the maximum rate is shifted significantly to correspond with a lower partition coefficient (0.59).

As expected, the variation in $X_{\mathrm{RaSO_4}}$ leads to very small changes both in $\beta(x)$ and $R_{hkl}^{B+S}(x)$. However, the maximum supersaturation value, $\beta(x)_{\max}$, corresponds to a solid solution composition $x_{\max}$, which is in thermodynamic equilibrium with respect to a *saturated* aqueous solution with the same aqueous activity composition as the current supersaturated solution (Prieto, 2009). Essentially, if a solid solution with composition $x_{\max}$ is crystallized from the supersaturated solution, the activity-based effective partition coefficient will equal the thermodynamic partition coefficient. On the other hand, the maximum growth rate, $R_{hkl}^{B+S}(x)_{max}$, corresponds to the solid solution composition that is most likely to precipitate from a kinetic point of view. As the system moves further from equilibrium the model predicts that these small variations in $\beta(x)$ and $R_{hkl}^{B+S}(x)$ will be reflected in significantly different partition coefficients (vertical dotted lines, Fig. 10). The difference between K''_D as predicted by $\beta(x)_{\max}$ (i.e., ~ 1.8) and $R_{hkl}^{B+S}(x)_{\max}$ represents a kinetic effect provoked by the higher growth rate associated with the more soluble solid solution composition (i.e., the one with less $\mathrm{RaSO_4}$).

The calculation of the growth rate exemplified above was carried out for all the experimental data and for both the B + S and BCF growth models. For each experimental data point (i.e., for each solution composition in Table 2) the value of $K''_{D,\mathrm{barite}}$, which corresponds to the maxima of the two growth models, was plotted against the degree of supersaturation with respect to pure barite (symbols, Fig. 11). For comparison, the empirical law and its uncertainty envelope (Eq. (10)) is presented by the solid and dashed lines. Note that the symbols in Fig. 11 represent the results of a theoretical model (Eqs. (11) and (12)) calculated using the solution compositions, while the solid lines represent an empirical equation (Eq. (10)) based on the experimental observations of the partition coefficient. The two sets of calculations are absolutely independent of each other. Despite the fact that the models presented in Eqs. (11) and (12) have large ambiguity, as the uncertainty of some of the parameters is large, the results of the birth and spread model show qualitatively a similar behavior to that of the experimental data for the decrease in $K''_{D,\mathrm{barite}}$ with the increase in β_{barite}. The results of the B + S model are further supported by the SEM images which showed the existence of this growth mechanism in the present study (Fig. 3). For the spiral growth model (BCF model) a maximum growth rate was calculated for pure barite (i.e., $K''_{D,\mathrm{barite}} = 0$) for all degrees of saturation above 1.5. Therefore, the BCF model does not agree with the experimental data. As noted above, the empirical law represents the bulk partition coefficient, while the growth models represent the partition coefficient on the (001) face.

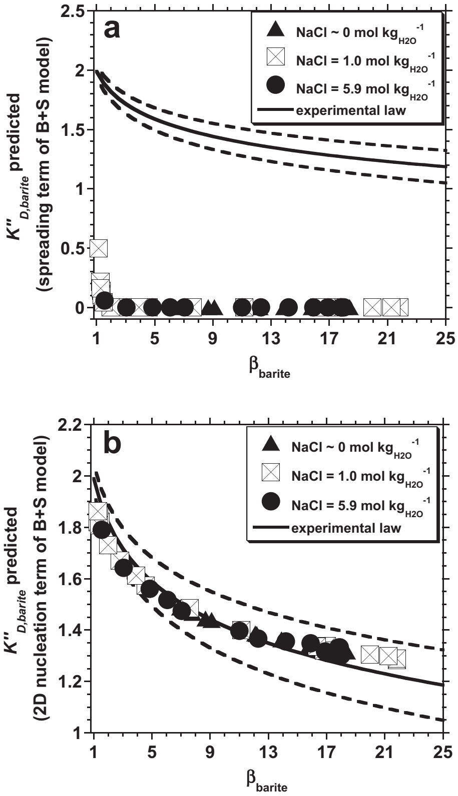

Fig. 12. The activity-based partition coefficient, $K''_{D,\mathrm{barite}}$, as a function of the degree of supersaturation with respect to barite, β_{barite}. Symbols are model results where for each data point the growth rate as a function of the solid composition was calculated according to: (a) the rate of spreading of 2D islands ($v_\infty(x)$, Eq. (18)), and (b) the nucleation rate of 2D islands ($I(x)$, Eq. (19)). The value of $K''_{D,\mathrm{barite}}$ for each calculation is the one which corresponds with the maximum of these rates. For the rate of spreading of 2D islands a maximum rate was calculated for pure barite (i.e., $K''_{D,\mathrm{barite}} = 0$). The solid and dashed lines in both plots are the empirical law and its uncertainty envelop (Eq. (10)).

The BCF model shares many of the concepts of surface diffusion and step advancement used in the birth and spread model. The main difference is that the BCF model proposes screw dislocations as continuous and self-perpetuating sources of kink sites, and therefore there are no significant energy barriers to be overcome (Pina et al., 2004a). For the birth and spread of two-dimensional islands model the nucleating island should have a critical radius (ρ_c) in order that the free energy of the system will decrease as a result of the growth (Ohara and Reid, 1973). Therefore, it is intriguing to further explore the results of the birth and spread of two-dimensional islands model.

The rate of birth and spread of two-dimensional islands, generalized here for the case of a solid solution, can be written as (Ohara and Reid, 1973):

$$R_{hkl}^{B+S}(x) = d_{hkl}(x) \cdot I_{hkl}(x)^{1/3} \cdot v_{\infty,hkl}(x)^{2/3} \tag{17}$$

where $I(x)$ is the rate of nucleation of critical nuclei (number of nuclei formed $\mathrm{m^{-2}\,s^{-1}}$) and $v_\infty(x)$ is the growth velocity ($\mathrm{m\,s^{-1}}$) of a straight step.

The expressions for $v_\infty(x)$ and $I(x)$ can be written as (Ohara and Reid, 1973):

$$v_{\infty,hkl}(x) = 2 \cdot D_S \cdot \frac{C_{SE,hkl}(x) \cdot V_{\mathrm{GU}}(x)}{d_{hkl}(x) \cdot X_{S,hkl}} \cdot (\beta(x) - 1) \tag{18}$$

and

$$I_{hkl}(x) = \frac{2}{\pi} \cdot n_{hkl}(x)^2 \cdot \bar{v} \cdot \sqrt{\frac{V_{\mathrm{GU}}(x) \cdot \ln\beta(x)}{d_{hkl}(x)}} \cdot \exp\left. \frac{-\pi \cdot d_{hkl}(x) \cdot (\sigma_{hkl}(x))^2 \cdot V_{\mathrm{GU}}(x)}{3 \cdot (k \cdot T)^2 \cdot \ln\beta(x)} \right) \tag{19}$$

The complete rate law for the birth and spread model (Eq. (11)) is derived by inserting Eqs. (18) and (19) into Eq. (17). The nucleation and growth rates, as predicted by Eqs. (18) and (19), were calculated for the range of the solid composition (X_{RaSO_4} in the range 0–1 × 10^{-7}) for each of the aqueous solutions in the experiments. For each experimental data point (i.e., for each solution composition in Table 2) the value of $K''_{D,\mathrm{barite}}$, which correspond with the maxima of either of these two terms ($I(x)_{\mathrm{max}}$ and $v_\infty(x)_{\mathrm{max}}$), is plotted against the degree of supersaturation with respect to pure barite (symbols, Fig. 12). As should be expected the values of K''_D calculated by the full rate law, $R^{B+S}_{hkl}(x)$, lie in between the values calculated by the spreading rate, $v_{\infty,hkl}(x)$, and the nucleation rate, $I_{hkl}(x)$ (compare Fig. 11a with Fig. 12a and b).

These calculations suggest that the spread of the islands show kinetic preference to incorporate Ra^{2+} only when $\beta_{\mathrm{barite}} < 2$ (Fig. 12a); that is, above this value $v_{\infty,hkl}(x)_{\mathrm{max}}$ is derived when $K''_D = 0$ ($X_{\mathrm{RaSO}_4} = 0$). On the other hand, the agreement between the values of K''_D derived by $I_{hkl}(x)_{\mathrm{max}}$ and the empirical law is remarkably good (Fig. 12b). Note that no fitting was applied when calculating Eq. (19).

The incorporation of Ra^{2+} into the barite lattice reduces the free energy barrier for nucleation. This can be justified by examining the expression for the critical free energy necessary to form a stable 2D nucleus (ΔG_c), generalized here for the case of a solid solution (Ohara and Reid, 1973):

$$\Delta G_C(x) = \frac{\pi \cdot d_{hkl}(x) \cdot (\sigma_{hkl}(x))^2 \cdot V_{\mathrm{GU}}(x)}{k \cdot T \cdot \ln\beta(x)} \tag{20}$$

This critical free energy expression is what forms the exponential term in Eq. (11). Clearly, as the supersaturation ratio is maximized with respect to a given solid solution composition (Fig. 10a), $\Delta G_c(x)$ is minimized and $R^{B+S}(x)$ increases; that is, the birth and spread model suggests that there is a thermodynamic preference to incorporate Ra^{2+} into the barite lattice through the nucleation of the 2D nuclei. This led us to test only the effect of the critical free energy term on the calculation of K''_D in the $\mathrm{Ra}_x\mathrm{Ba}_{1-x}\mathrm{SO}_4$ system. We found that the results presented in Fig. 12b can be reproduced by considering only the maximum values of the exponential term of Eq. (19) (i.e., when $\Delta G_c(x)$ is minimized, Eq. (20)).

It is apparent that the activity-based partition coefficient for Ra in barite can be excellently estimated for a given solution composition using the free energy for nucleation of 2D nuclei. That is:

$$K''_D = \frac{x_{\mathrm{max}}/(1 - x_{\mathrm{max}})}{[\mathrm{Ra}]/[\mathrm{Ba}]}; \tag{21}$$

where x_{max} maximizes the function $\exp(-\Delta G_c(x)/3k\cdot T)$.

The excellent agreement between the theoretical approach presented by Eq. (21) and the experimental data raises two concerns. Firstly, poly-nucleation of 2D nuclei is probably not sufficient for the growth of the barite crystal, and the nuclei are probably supported by a substantial spreading. As discussed above, the theoretical calculations of the spreading stage do not support the portioning of Ra^{2+}. Secondly, as the precipitation reaction approaches equilibrium nucleation rates should decrease and become non-significant. Therefore, the excellent agreement between Eq. (21) and the experimental law is somewhat surprising when the reaction approaches equilibrium. These concerns indicate that, even though 2D nucleation growth mechanism seems to control the partitioning the partition of Ra^{2+} into barite, further improvements of the generalized B + S model are still required.

5. CONCLUDING REMARKS

The present study systematically investigated the precipitation kinetics of the $\mathrm{Ra}_x\mathrm{Ba}_{1-x}\mathrm{SO}_4$ solid solution from aqueous solutions up to 5.9 mol $\mathrm{kgH_2O}^{-1}$ NaCl, at circum-neutral pH and at ambient temperature. The main findings of this study are:

1. The composition of the $\mathrm{Ra}_x\mathrm{Ba}_{1-x}\mathrm{SO}_4$ solid solution which precipitates is partly affected by the ionic strength of the solution, as a result of non-equal changes in the chemical potential of dissolved Ra^{2+} and Ba^{2+} cations. This is demonstrated by a decrease in the concentration-based partition coefficient. The ionic strength effect can be compensated for by calculating the activity-based partition coefficient.
2. The composition of the $\mathrm{Ra}_x\mathrm{Ba}_{1-\mathrm{x}}\mathrm{SO}_4$ solid solution which precipitates is mainly affected by the precipitation kinetics of the solid solution. This is demonstrated by a decrease in the activity-based partition coefficient, which decreases as the degree of supersaturation of the solution with respect to barite increases. The following empirical law describes the dependency of the activity-based partition coefficient, K_D, barite″, on the degree of supersaturation, β_{barite}:[K_D, barite″ = (1.99 ± 0.05) − (0.58± 0.06) · log(β_{barite}).] This empirical law adequately describes literature data of much higher complexity, both from laboratory experiments and field observations.
3. Because of the low solubility of barite, aqueous solutions can easily become supersaturated with respect to this phase. Therefore, it should be expected that the precipitation of the $\mathrm{Ra}_x\mathrm{Ba}_{1-\mathrm{x}}\mathrm{SO}_4$ solid solution will commence under non-equilibrium conditions. At such circumstances a distribution model, which describes the precipitation of the $\mathrm{Ra}_x\mathrm{Ba}_{1-\mathrm{x}}\mathrm{SO}_4$ solid solution with a constant partition coefficient is not appropriate, and can lead to orders of magnitude differences in the estimated Ra concentrations.
4. Co-precipitation of Ra and Ba in barite has been established as an important process that has the potential to control Ra concentration (Bruno et al., 2007; Bosbach, 2010). However, in safety analysis, when worst case sce-

narios are due to be assessed, a value of 1.0 for the effective partition coefficient is appropriate for estimating the maximum expected Ra concentration.

5. Finally, the experimental results are described quantitatively by a theoretical model that considers the critical free energy for 2D nucleation to be a function of the solid composition. This is in agreement with the literature showing that the birth and spread of 2D islands is a dominant growth mechanism in barite.

ACKNOWLEDGEMENTS

This study was supported by THE ISRAEL SCIENCE FOUNDATION (grant #511/09). Y.O. Rosenberg is supported by the Adams Fellowship Program of the Israel Academy of Sciences and Humanities and is also grateful to the Rieger Foundation's JNF Program for Environmental Studies and the Water Authority of Israel for their generous support. The authors would like to thank our colleagues Frank Heberling, Dieter Schild and Eva Soballa for technical assistance during the XRD and SEM-EDX analyses. The authors appreciate the thorough review of two anonymous reviewers and of Prof. Manuel Prieto, and would also like to thanks Prof. Robert H. Byrne for serving as the associate editor.

REFERENCES

Astilleros J. M., Pina C. M., Ferna´ndez-Dı´az L. and Putnis A. (2003) Supersaturation functions in binary solid solution–aqueous solution systems. *Geochim. Cosmochim. Acta* **67**, 1601–1608.

Blount C. W. (1977) Barite solubilities and thermodynamic quantities up to 300 °C and 1400 bars. *Am. Mineral.* **62**, 942–957.

Bosbach D. (2002) Linking molecular scale barite precipitation mechanisms with macroscopic reaction rates. In *Water–Rock Interactions, Ore Deposits, and Environmental Geochemistry: A Tribute to David A. Crerar. Geochemical Society Special Publication* (eds. R. Hellmann and S. A. Wood). The Geochemical Society, St. Louis.

Bosbach D. (2010) Solid-solution formation and the long-term safety of nuclear-waste disposal. In *EMU Notes in Mineralogy* (eds. M. Prieto and H. Stoll). European Mineralogical Union and the Mineralogical Society of Great Britain & Ireland, London.

Bosbach D., Hall C. and Putnis A. (1998) Mineral precipitation and dissolution in aqueous solution: *In situ* microscopic observations on barite (001) with atomic force microscopy. *Chem. Geol.* **151**, 143–160.

Bruno J., Bosbach D., Kulik D. and Navrotsky A. (2007) *Chemical thermodynamics of solid solutions of interest in radioactive waste management*. OECD Publishing, Paris.

Burton W. K., Cabrera N. and Frank F. C. (1951) The growth of crystals and the equilibrium structure of their surfaces. *Philos Trans R Soc Lond* **243**, 299–358.

Curti E. (1999) Coprecipitation of radionuclides with calcite: estimation of partition coefficients based on a review of laboratory investigations and geochemical data. *Appl. Geochem.* **14**, 433–445.

Curti E., Fujiwara K., Iijima K., Tits J., Cuesta C., Kitamura A., Glaus M. A. and Mu¨ller W. (2010) Radium uptake during barite recrystallization at 23 ± 2 °C as a function of solution composition: an experimental 133Ba and 226Ra tracer study. *Geochim. Cosmochim. Acta* **74**, 3553–3570.

Doerner H. A. and Hoskins W. M. (1925) Co-precipitation of radium and barium sulfates. *J. Am. Chem. Soc.* **47**, 662–675.

Gordon L. and Rowley K. (1957) Coprecipitation of radium with barium sulfate. *Anal. Chem.* **29**, 34–37.

Hamlat M. S., Kadi H. and Fellag H. (2003) Precipitate containing norm in the oil industry: modelling and laboratory experiments. *Appl. Radiat. Isot.* **59**, 95–99.

Hartman P. and Strom C. S. (1989) Structural morphology of crystals with the barite ($BaSO_4$) structure: a revision and extension. *J. Cryst. Growth* **97**, 502–512.

Harvie C. E., Moller N. and Weare J. H. (1984) The prediction of mineral solubilities in natural waters: the Na–K–Mg–Ca–H–Cl–SO_4–OH–HCO_3–CO_3–CO_2–H_2O system to high ionic strengths at 25 °C. *Geochim. Cosmochim. Acta* **48**, 723–751.

He S., Oddo J. E. and Tomson M. B. (1995) The nucleation kinetics of barium sulfate in NaCl solutions up to 6 m and 90 °C. *J. Colloid Interface Sci.* **174**, 319–326.

Hill R. J. (1977) A further refinement of the barite structure. *Can. Mineral.* **15**, 522–526.

Hina A. and Nancollas G. H. (2000) Precipitation and dissolution of alkaline earth sulfates: kinetics and surface energy. *Rev. Mineral. Geochem.* **40**, 277–301.

Kim G., Burnett W. C., Dulaiova H., Swarzenski P. W. and Moore W. S. (2001) Measurement of ^{224}Ra and ^{226}Ra activities in natural waters using a radon-in-air monitor. *Environ. Sci. Technol.* **35**, 4680–4683.

Langmuir D. and Riese A. C. (1985) The thermodynamic properties of radium. *Geochim. Cosmochim. Acta* **49**, 1593–1601.

Marques B. E. (1934) La Pre´cipitation Fractionne´e du Sulfate de Baryum Radife`re. *C R Acad. Sci.* **198**, 1765–1767.

McIntire W. L. (1963) Trace element partition coefficients – a review of theory and applications to geology. *Geochim. Cosmochim. Acta* **27**, 1209–1264.

Monnin C. and Galinier C. (1988) The solubility of celestite and barite in electrolyte solutions and natural waters at 25 °C: a thermodynamic study. *Chem. Geol.* **71**, 283–296.

Moore W. S. (2008) Fifteen years experience in measuring ^{224}Ra and ^{223}Ra by delayed-coincidence counting. *Mar. Chem.* **109**, 188–197.

Ohara M. and Reid R. (1973) *Modeling Crystal Growth Rates from Solution*. Prentice-Hall.

Parkhurst, D. L. and Appelo, C. A. J. (1999) PHREEQC 2.15 a computer program for speciation, batch-reaction, one-dimentional transport and inverse geochemical calculation. Water-Resources Investigation Report 99–4259. U.S. Geological Survey.

Paytan A., Moore W. S. and Kastner M. (1996) Sedimentation rate as determined by ^{226}Ra activity in marine barite. *Geochim. Cosmochim. Acta* **60**, 4313–4319.

Pina C. M., Becker U., Risthaus P., Bosbach D. and Putnis A. (1998) Molecular-scale mechanisms of crystal growth in barite. *Nature* **395**, 483–486.

Pina C. M., Enders M. and Putnis A. (2000) The composition of solid solutions crystallising from aqueous solutions: the influence of supersaturation and growth mechanisms. *Chem. Geol.* **168**, 195–210.

Pina C. M. and Jordan G. (2010) Reactivity of mineral surfaces at nano-scale: kinetics and mechanisms of growth and dissolution. *EMU Notes Mineral.* **8**, 239–323.

Pina C. M. and Putnis A. (2002) The kinetics of nucleation of solid solutions from aqueous solutions: a new model for calculating non-equilibrium distribution coefficients. *Geochim. Cosmochim. Acta* **66**, 185–192.

Pina C. M., Putnis A. and Astilleros J. M. (2004a) The growth mechanisms of solid solutions crystallising from aqueous solutions. *Chem. Geol.* **204**, 145–161.

Pina C. M., Putnis C. V., Becker U., Biswas S., Carroll E. C., Bosbach D. and Putnis A. (2004b) An atomic force microscopy and molecular simulations study of the inhibition of barite growth by phosphonates. *Surf. Sci.* **553**, 61–74.

Pitzer K. S. (1991) Ion interaction approach: theory and data correlation. In *Activity Coefficients in Electrolyte Solutions* (ed. Kenneth S. Pitzer), second ed. CRC Press, Boca Raton, Florida.

Prieto M. (2009) Thermodynamics of solid solution–aqueous solution systems. In *Thermodynamics and Kinetics of Water–Rock Interaction* (eds. E. H. Oelkers and J. Schott). Reviews in Mineralogy and Geochemistry.

Prieto M., Putnis A. and Fernandez-Diaz L. (1993) Crystallization of solid solutions from aqueous solutions in a porous medium: zoning in (Ba, Sr) SO_4. *Geol. Mag.* **130**, 289–299.

Risthaus P., Bosbach D., Becker U. and Putnis A. (2001) Barite scale formation and dissolution at high ionic strength studied with atomic force microscopy. *Colloids Surf., A* **191**, 201–214.

Rosenberg Y. O., Metz V. and Ganor J. (2011a) Co-precipitation of radium in high ionic strength systems: 1. Thermodynamic properties of the Na–Ra–Cl–SO_4–H_2O system-estimating Pitzer parameters for $RaCl_2$. *Geochim. Cosmochim. Acta* **75**, 5389–5402.

Rosenberg Y. O., Metz V. and Ganor J. (2013) Radium removal in a large scale evaporitic system. *Geochim. Cosmochim. Acta* **103**, 121–137.

Rosenberg Y. O., Metz V., Oren Y., Volkman Y. and Ganor J. (2011b) Co-precipitation of radium in high ionic strength systems: 2. Kinetic and ionic strength effects. *Geochim. Cosmochim. Acta* **75**, 5403–5422.

Söhnel O. (1982) Electrolyte crystal–aqueous solution interfacial tensions from crystallization data. *J. Cryst. Growth* **57**, 101–108.

Söhnel O. and Mullin J. W. (1988) Interpretation of crystallization induction periods. *J. Colloid Interface Sci.* **123**, 43–50.

van Beek P., Reyss J. L., DeMaster D. and Paterne M. (2004) ^{226}Ra-in marine barite: relationship with carbonate dissolution and sediment focusing in the equatorial pacific. *Deep Sea Res. Part I* **51**, 235–261.

Wang Y. and Xu H. (2001) Prediction of trace metal partitioning between minerals and aqueous solutions: a linear free energy correlation approach. *Geochim. Cosmochim. Acta* **65**, 1529–1543.

Watson E. B. (2004) A conceptual model for near-surface kinetic controls on the trace-element and stable isotope composition of abiogenic calcite crystals. *Geochim. Cosmochim. Acta* **68**, 1473–1488.

Weigel F. and Trinkel A. (1968) Zur Kristallchemie des Radimus, II. Radiumsalze vom Typ RaXO4. *Radiochim. Acta* **9**, 140–144.

Zhu C. (2004) Coprecipitation in the barite isostructural family: 1. Binary mixing properties. *Geochim. Cosmochim. Acta* **68**, 3327–3337.